nature communications

Article

https://doi.org/10.1038/s41467-025-64158-8

A basal body microtubule singlet-to-doublet transition in *Plasmodium* male gametogenesis

Received: 29 April 2025

Accepted: 9 September 2025

Published online: 15 October 2025

Check for updates

Shuzhen Yang[1,4], Shanshan Ma[2,4], Chengxian Yuan[1,4], Zhixun Li[2], Fanbiao Ji[1], Luming Yao[1], Huiting Cui[1] ✉, Qiang Guo[2,3] ✉ & Jing Yuan[1] ✉

Axoneme assembly constitutes a pivotal process in male gametogenesis of *Plasmodium*. *Plasmodium* possesses a unique nuclear envelope-anchored basal body that templates axoneme assembly, distinct from the basal body that templates the axoneme of cilia or flagella to protrude from the cell surface. In the canonical basal body, the microtubule (MT) triplet extends and forms the axonemal MT doublet. However, this characteristic MT triplet has not been detected in *Plasmodium*. Indeed, the MT organization and the mechanism underlying the axonemal MT doublet assembly remain elusive in *Plasmodium*. Here we utilize high-resolution imaging methods including iterative ultrastructure expansion microscopy (iU-ExM) and cryo-electron tomography (cryo-ET) to resolve the native MT organization in the basal body of male gametes from the rodent malaria parasite *P. yoelii*. The parasite exhibits an MT singlet-to-doublet transition, distinct from the canonical MT triplet-to-doublet transition. Furthermore, we reveal that δ-Tubulin and ε-Tubulin are expressed in male gametocytes and regulate axoneme formation during male gametogenesis. δ-Tubulin is localized at the proximal end of the MT B-tubule and modulates B-tubule assembly of MT doublet. Our work provides the native architecture of MT singlet-to-doublet transition and reveals the key role of δ-Tubulin and ε-Tubulin in MT singlet-to-doublet transition in the basal body of *Plasmodium*.

Malaria is a mosquito-borne disease caused by protozoan parasites of the genus *Plasmodium*, resulting in 263 million cases of infection and 597,000 deaths in 2023[1]. Malaria parasites are transmitted by female *Anopheles* mosquitoes during their blood meal. In vertebrate hosts, *Plasmodium* undergoes asexual proliferation in the liver and then in erythrocytes, where a small portion of the parasites differentiate sexually into male and female gametocytes. After being ingested into the midgut during a mosquito bite, male and female gametocytes are activated and differentiate into male and female fertile gametes, a process known as gametogenesis[2,3]. While a female gametocyte produces a female gamete, a male gametocyte gives rise to eight flagellated male gametes. A male gamete fertilizes a female gamete to form a zygote. Following the development of the zygote, ookinete, oocyst, and sporozoite stages in mosquitoes, the parasites are ultimately injected from the salivary gland into a mammalian host, completing the transmission of the malaria parasite[4].

Male gametogenesis in *Plasmodium* is an extraordinarily rapid cell proliferation process. In 10–12 min, eight simple uniflagellate haploid

[1]State Key Laboratory of Cellular Stress Biology, School of Life Sciences, Faculty of Medicine and Life Sciences, Xiamen University, Xiamen, China. [2]State Key Laboratory of Membrane Biology, Peking-Tsinghua Center for Life Sciences, Academy for Advanced Interdisciplinary Studies, School of Life Sciences, Peking University, Beijing, China. [3]Changping Laboratory, Beijing, China. [4]These authors contributed equally: Shuzhen Yang, Shanshan Ma, Chengxian Yuan. ✉e-mail: cuihuiting@xmu.edu.cn; guo.qiang@pku.edu.cn; yuanjing@xmu.edu.cn

male gametes that contain only a nucleus, an axoneme and a basal body are developed from a male gametocyte[5]. This process is coordinated by two spatially distinct components. One is the basal body (BB)-directed assembly of eight axonemes in the cytoplasm. Initially, a tetrad of BBs assembles in association with the nucleus. This tetrad quickly serves as a template for rapid axoneme assembly[3,6]. Through one round of duplication and three rounds of continuous separation, eight discrete BB-axoneme structures form[6,7]. The other constitutes three rounds of chromosome duplication without nuclear division, leading to the formation of an octoploid nucleus[8,9]. Intriguingly, a nuclear envelope-crossing bipartite microtubule organization center (MTOC) orchestrates both processes through the assembly of two distinct microtubule (MT) structures, the spindle and the axoneme[10]. Within the bipartite MTOC, the cytoplasmic BB acts as the nucleation template for the axoneme, while the nuclear spindle pole serves as the template for the spindle[11]. Subsequently, the BB-axoneme structures, in association with a haploid nucleus, exflagellate from the cell body of male gametocytes, yielding eight uniflagellate haploid male gametes.

In eukaryotes, the axoneme serves as the structural core underpinning the motility of the hair-like organelles flagellum and cilia[12]. The axoneme is a conserved structure, featuring an organized arrangement of MTs in the canonical "9 + 2" pattern: nine sets of peripheral linked MT doublets (A-B tubules) surrounding a central pair of MT singlets[13]. BB functions as an MTOC, nucleating and anchoring the axoneme for growth[14,15]. Characteristically, the BB exhibits a barrel-shaped structure with ninefold symmetrical MT triplets (A-B-C tubules)[16]. During axoneme assembly, the A-B tubules of the MT triplet in the BB extend, forming the axonemal MT doublet. This process showcases the canonical "MT triplet-to-doublet transition" observed in the flagellum and cilia[17].

In the life cycle of *Plasmodium*, the male gamete represents the sole parasite stage equipped with an axoneme. Despite the axoneme's conserved structure and function[18], the BB biogenesis and dynamics in *Plasmodium* differ remarkably from the canonical BB. First, a canonical BB arises from the transformed centriole during the cell cycle[19]. In *Plasmodium*, the BB is assembled de novo at the cytoplasmic side of the nuclear envelope, and eight BBs are finally formed via duplication[20]. Second, a canonical BB anchors underneath the plasma membrane, and the axoneme extends from the cell surface, pushing the plasma membrane out[14]. In *Plasmodium*, eight nuclear envelope-anchored BBs direct the assembly of eight axonemes in the cytoplasm. Third, *Plasmodium* possesses a dynamic localization of BB, distinct from the stationary localization of canonical BB. The BB detaches from the nuclear envelope after the cytoplasmic assembly of eight axonemes. Each BB-axoneme structure couples a haploid nucleus and egresses from the gametocyte cell body via exflagellation. The differences in BB biogenesis and behavior imply that *Plasmodium* may have evolved a novel structure of BB compared to canonical forms. Consistent with this hypothesis, previous electron microscopy studies failed to detect the characteristic MT triplet in the BB of the *Plasmodium* male gametes[6]. Instead, MT singlets appeared in the blurred images obtained under limited resolutions[3,6,21]. These results suggest a *Plasmodium* axonemal MT transition pattern different from the well-known "MT triplet-to-doublet transition". So far, the fine and native structure of MT formation and transition in the BB of the *Plasmodium* male gametes remains unclear. Furthermore, the mechanism underlying the BB-templated axonemal MT formation in the absence of detectable MT triplet in the *Plasmodium* is not known.

Delta-tubulin (δ-Tub) and epsilon-tubulin (ε-Tub) are the non-canonical members of the tubulin superfamily[22]. The *δ-tub* and *ε-tub* genes exist only in the organisms comprising the MT triplets in the BB or centriole, suggesting their roles in MT triplet assembly during BB or centriole biogenesis[22,23]. Consistently, δ-Tub or ε-Tub deficiency causes defects in MT triplet formation in BB or centriole assembly[24–26], and thus impairs BB-templated cilia formation or centrosome-mediated mitosis[27–29]. However, the precise localizations and functions of δ-Tub and ε-Tub within the BB remain elusive. Interestingly, despite the absence of detectable MT triplets in the BB, both *δ-tub* and *ε-tub* genes are encoded in the *Plasmodium* species[30]. Transcriptome profiles revealed specific transcription of *δ-tub* and *ε-tub* in male gametocytes of *P. falciparum*, *P. berghei*, and *P. yoelii*[31–33]. A recent pooled parasite-based genetic screen revealed that deletion of *ε-tub* reduced male fertility while deletion of *δ-tub* had no effect on male fertility in *P. berghei*[34]. So far, the functional requirements of δ-Tub and ε-Tub in axoneme formation during male gametogenesis remain elusive in *Plasmodium*.

In this study, we utilize high-resolution imaging methods, including transmission electron microscopy (TEM), iterative ultrastructure expansion microscopy (iU-ExM), and cryo-electron tomography (cryo-ET), to resolve the native MT organization in the BB of male gametes from the rodent malaria parasite *P. yoelii*. We discover that *P. yoelii* exhibits an MT singlet-to-doublet transition pattern in the BB for axonemal MT assembly, distinct from the canonical MT triplet-to-doublet transition. Furthermore, we reveal that δ-Tub and ε-Tub are expressed explicitly in male gametocytes and regulate axoneme formation during the male gametogenesis. δ-Tub is localized at the B-tubule proximal end of the MT doublet and modulates the B-tubule assembly of the MT doublet.

Results

Microtubule singlet-to-doublet transition in basal body of *P. yoelii* male gametes

To investigate the BB in the male gametes of *Plasmodium*, we generated the *P. yoelii* (17XNL strain) parasite line *sas4::6HA*, in which the BB protein SAS4 was endogenously tagged with a sextuple hemagglutinin epitope (6HA) at the carboxyl (C)-terminus. The male gametes were stained with antibodies against HA and α/β-Tubulin and subjected to iU-ExM, an improved U-ExM-based super-resolution microscopy imaging method recently developed[35]. As expected, SAS4 was localized in the BB of male gametes (Fig. 1A)[21]. Notably, the BBs were thinner than the axonemes (Fig. 1A), with an average diameter of 165 ± 12 nm for BBs and 234 ± 12 nm for axonemes (Fig. 1B). This ratio of thinner BB over axoneme in *P. yoelii* is distinct from that in the cilia-containing organisms, including the green algae *Chlamydomonas reinhardtii* (*C. reinhardtii*)[36]. *C. reinhardtii* possesses a canonical MT triplet-to-doublet transition in the BB of flagella[36] and is a common model for BB or centriole biology[37]. For a direct comparison, we analyzed the BB structure in the *C. reinhardtii*. iU-ExM showed that the diameter of BB (226 ± 7 nm) is larger than that of the axoneme (202 ± 9 nm) in *C. reinhardtii* (Fig. 1C, D). Cross-section images of iU-ExM showed that the *P. yoelii* axonemes had a ninefold symmetrical distribution of MTs (Fig. 1E), in agreement with previous observations[38]. However, the BB appeared with fewer distinct MTs and did not have a ninefold symmetry in *P. yoelii* (Fig. 1E). Compared to *P. yoelii*, *C. reinhardtii* showed a ninefold symmetry of MTs in both BB and axoneme (Fig. 1F), consistent with previous observations[35].

We used TEM to investigate the MT organization in the BB of *P. yoelii* male gametes. Longitudinal section images showed that the BB was more electron-dense but less organized compared to the axoneme (Fig. 1G). In the cross-section images, nine or fewer MT singlets corresponding to the A-tubule were detected in the BBs (Fig. 1H-1 and Supplementary Fig. 1A). No MT triplets were observed in the BBs, consistent with the previous observations[3]. In the distal area of BB, MT singlets and doublets co-existed (Fig. 1H-2, H-3 and Supplementary Fig. 1A). Ninefold symmetrical MT doublets and a central pair of MT singlets appear from the BB transition area to the axoneme, displaying the "9 + 2" MT pattern (Fig. 1H-4). In the TEM images, the diameter of BB (175 ± 8 nm) is smaller than that of axoneme (234 ± 8 nm) (Fig. 1I), consistent with the results of iU-ExM in Fig. 1B. These results demonstrated that the axonemal MT doublets grow

https://doi.org/10.1038/s41467-025-64158-8

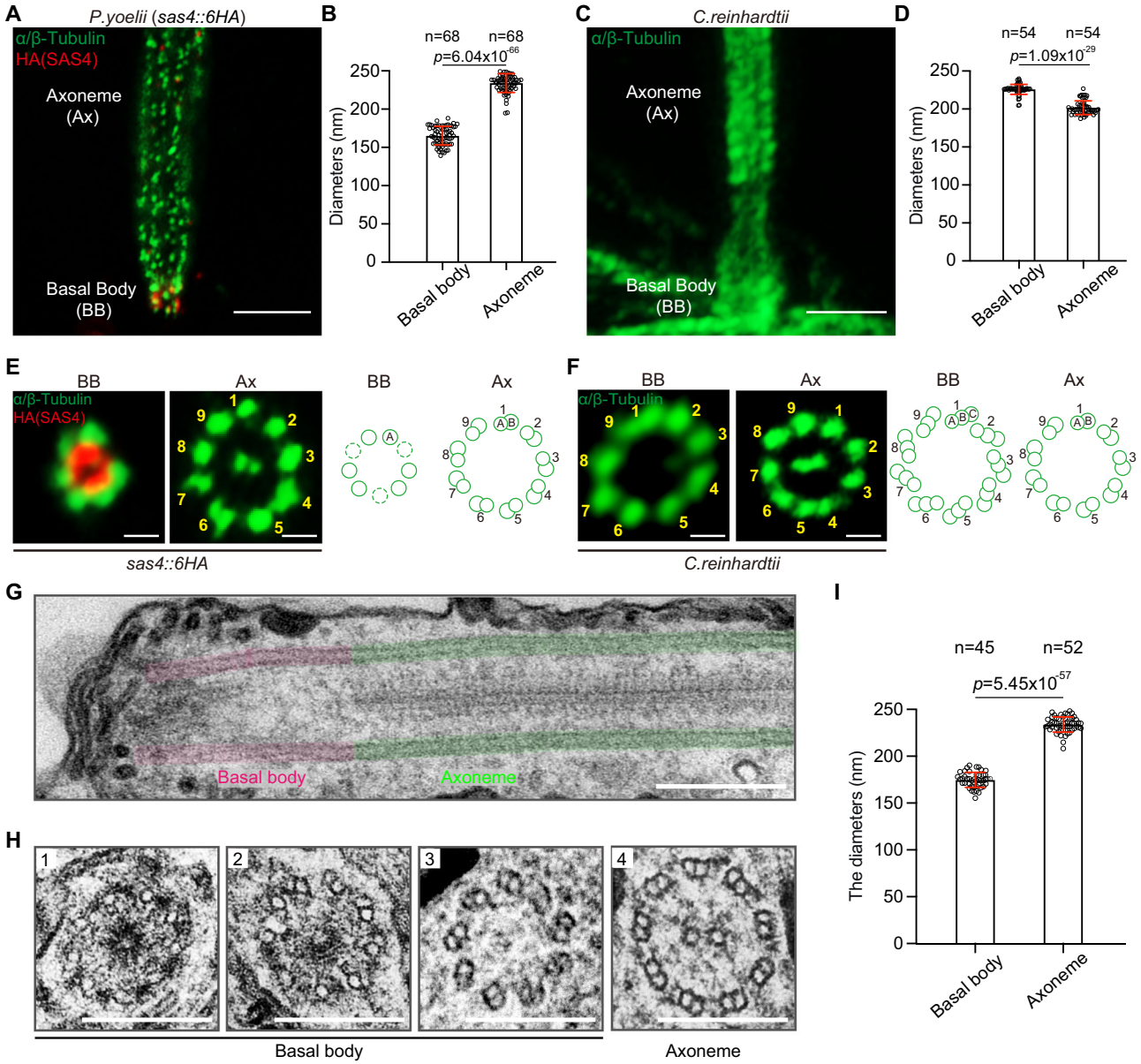

Fig. 1 | MT singlet-to-doublet transition in basal body of *P. yoelii* male gametes. **A** Iterative ultrastructure expansion microscopy (iU-ExM) of male gamete in the *sas4::6HA* line of the *P. yoelii* parasite. SAS4 is a basal body marker protein. Parasites were stained with antibodies against HA and α/β-Tubulin. A representative from three independent experiments. Scale bars = 5 µm. The expansion factor is 16 ± 0.5. **B** Diameter of basal body and axoneme from *P. yoelii* in (**A**). *n* is the number of male gametes measured. Values are Mean ± SD, two-tailed *t*-test. **C** iU-ExM of flagellum in the *C. reinhardtii*. Cells were stained with antibodies against α/β-Tubulin. A representative from three independent experiments. Scale bars = 5 µm. The expansion factor is 16 ± 0.5. **D** Diameter of the basal body and axoneme from *C. reinhardtii* in (**C**). *n* is the number of flagellums measured. Values are Mean ± SD, two-tailed *t*-test. **E**, **F** iU-ExM cross-sections of the basal body and axoneme in the *P. yoelii sas4::6HA* parasites (**E**) and *C. reinhardtii* (**F**). A representative from three independent experiments. Scale bars = 1 µm. Right panels show the schematic of MT structures in the basal body and axoneme. The dotted line cycle refers to the missing MT singlets in the cross-section image of the basal body. **G** Transmission electron microscope (TEM) showing the MTs of the basal body (red) and axoneme (green) in male gamete of the *P. yoelii* 17XNL parasite. A representative from three independent experiments. Scale bars = 250 nm. **H** TEM cross sections of MT singlets and doublets in the basal body and axoneme of *P. yoelii* gametes. A representative from three independent experiments. Scale bars = 200 nm. **I** Diameter of the basal body and axoneme in *P. yoelii* in (**H**). *n* is the number of basal bodies and axonemes measured. Values are Mean ± SD, two-tailed *t*-test. Source data are provided as a Source Data file.

from the MT singlets in the BB. This MT singlet-to-doublet transition in the *P. yoelii* BB differs from the MT triplet-to-doublet transition in canonical BBs.

To further confirm the MT singlet-to-doublet transition in the *P. yoelii* BB, we stained the 17XNL male gametes with an antibody targeting polyglutamylated tubulin (PolyE), which specifically labeled the B-tubule of mature MT doublet[39]. We stained *C. reinhardtii* flagella and *P. yoelii* male gametes with antibodies against α/β-Tubulin and PolyE, confirming the specific labeling of B-tubule in MT doublets by PolyE under iU-ExM (Supplementary Fig. 2A–C). Next, we used PolyE as a marker of the B-tubules to analyze the assembly dynamics of MT doublets during the early biogenesis of BB and axoneme in male gametogenesis. At 1 min post activation (mpa) of male gametocytes, we detected the aggregation of α/β-Tubulin signal while no PolyE signal appeared, suggesting the formation of BB containing only MT singlet. At 2 mpa, PolyE signal appeared and was mainly colocalized with α/β-Tubulin signal at the BB area (Supplementary Fig. 2D, E), indicating the formation of BB or axonemal MT doublets.

We generated another *P. yoelii* parasite line *sas4::4Myc* with endogenous SAS4 tagged with 4Myc at the C-terminus. At 1 mpa, SAS4 was concentrated in the BB of male gametocytes (Supplementary Fig. 3A), similar to previous observations[21]. However, no PolyE signal was detected in the BB (Supplementary Fig. 3A). At 2 mpa, the PolyE appeared and was localized close to SAS4 (Supplementary Fig. 3A), consistent with the PolyE localization dynamic in 17XNL (Supplementary Fig. 2D, E). We further analyzed the spatial relation between SAS4 and PolyE using U-ExM. We found that the SAS4-labeled BB is PolyE negative (Supplementary Fig. 3B). These results indicated that the *P. yoelii* male gamete possesses MT singlets in BB and the axonemal MT doublets grow from the MT singlets (Supplementary Fig. 3C).

Cryo-electron tomography of MT singlet-to-doublet transition

Next, we performed cryo-ET to visualize the in situ 3D organization of the MT singlet-to-doublet transition in BB of the *P. yoelii* 17XNL male gametes. A total of 19 tomograms were collected and utilized to trace the MTs. The canonical BB or centriole is characterized by a ninefold symmetrical arrangement of MT triplets, forming a cylinder or barrel-like structure[16]. We presented two tomograms in Fig. 2A and D. The BB in the *P. yoelii* male gametes displayed a polarized funnel shape (Fig. 2A, B, D, and E), differing from the canonical BBs[17]. Less than nine MT singlets were detected in the proximal end, while nine MT singlets emerged in the distal part of the BBs (see the blue A-tubules in Fig. 2B, C, E, and F). The proximal extremity of the MT singlets (A-tubules) was found at different heights to the BB proximal tip (Fig. 2B and E). In addition, the ninefold symmetrical arrangement was not detected for these MT singlets (Fig. 2C, F, and G). In the proximal to distal region of BB, the B-tubule is built on the MT singlets, developing into the MT doublets. Notably, the initiation of B-tubule assembly displays temporal asynchrony for the nine MT doublets (Fig. 2G). We measured the distance of proximal ends between A-tubule and B-tubule, which ranged from 60 to 600 nm (Fig. 2H). Eventually, all nine MT singlets obtain the B-tubules, displaying a ninefold symmetrical arrangement of MT doublets for axoneme growth (Fig. 2C, F, and G). Moreover, the assembly position of two central MT singlets also varied along the proximal to distal axis of BB (Fig. 2C, F, and G). We presented three other tomograms in Supplementary Fig. 4. These results of cryo-ET are also consistent with those from TEM and iU-ExM analysis.

Detailed cryo-ET images showed that the A-tubules appeared closed at their proximal end in the MT doublets (Fig. 2I). As an MTOC, the gamma-tubulin ring complex (γ-TuRC) is well known to nucleate the MT singlet at the minus end in eukaryotes[40], and it is thought to contribute to the assembly of A-tubules in the MT triplets of BB[41]. Therefore, the cap-like signal observed at the proximal end of the A-tubules likely corresponds to the γ-TuRC at the minus end of MTs. In contrast, the B-tubules were uncapped at the proximal end (Fig. 2I and Supplementary Fig. 5A, B), similar to the B- and C-tubules in MT triplets in canonical BB[41]. These results also suggested that the nucleating mechanism of the B-tubule differs from the A-tubule in the MT doublets (Fig. 2J).

Taken together, the *P. yoelii* male gamete displays an MT singlet-to-doublet transition in BB for axonemal MT doublet formation. In addition, the MT A-tubules in the BB are not arranged symmetrically. Both A-tubules and B-tubules are initially assembled at variable heights in the BB. These features are significantly different from that of the MT organization in the canonical BBs[17].

δ-Tub is localized at the basal body of activated male gametocytes

δ-Tub and ε-Tub are involved in the MT triplet assembly during the BB or centriole formation, although their precise functions are unclear[22–26]. Despite the absence of MT triplet in the BB of *P. yoelii*, both *δ-tub* and *ε-tub* genes are encoded in all *Plasmodium* species[30]. So far, the functions of δ-Tub and ε-Tub remain elusive in *Plasmodium*. Previous transcriptome analyses detected the transcripts of *δ-tub* and *ε-tub* genes specifically in male gametocytes of *P. falciparum* and *P. berghei*[31,32]. We asked whether δ-Tub and ε-Tub play roles in the MT singlet-to-doublet transition of BB during male gametogenesis of *Plasmodium*. We investigated the expression of δ-Tub and ε-Tub in the parasite's life cycle. Using CRISPR-Cas9[42], the endogenous δ-Tub (PY17X_0838000) and ε-Tub (PY17X_1304100) were tagged with a 6HA at the C-terminus in the *P. yoelii* 17XNL strain (wildtype), generating two tagged parasite lines *δ-tub::6HA* and *ε-tub::6HA*. Immunofluorescence assay (IFA) revealed that δ-Tub was specifically expressed in gametocytes, but not in other stages, including the asexual blood stages in mice, midgut oocysts, and salivary gland sporozoites in mosquitoes (Fig. 3A). However, the IFA signal of ε-Tub was not detected in any stages of the *ε-tub::6HA* parasites. Immunoblot detected the gametocyte-specific expression of δ-Tub and ε-Tub (Supplementary Fig. 6A, B). Strikingly, ε-Tub displayed a significantly lower expression than δ-Tub (Supplementary Fig. 6A, B). To further analyze ε-Tub expression, we tagged the ε-Tub with a 6HA at the N-terminus. The resulting parasite line *6HA::ε-tub* still exhibited no detectable IFA signal of ε-Tub in the gametocytes. To compare protein levels directly within one parasite, we tagged δ-Tub with a 6HA in the *ε-tub::6HA* parasite and obtained a double-tagged parasite clone *ε-tub::6HA;δ-tub::6HA* (*DTS1*). Immunoblot detected the expression of both δ-Tub and ε-Tub in the *DTS1* gametocytes, with a sevenfold lower level for ε-Tub than δ-Tub (Supplementary Fig. 6C). These results demonstrated that both δ-Tub and ε-Tub are expressed in gametocytes; however, the expression level of ε-Tub is too low to be detected via IFA. Therefore, we solely analyzed the localization of δ-Tub in the following experiments.

To dissect the gender expression of δ-Tub, the *δ-tub::6HA* gametocytes were stained with antibodies recognizing α-Tubulin I and α-Tubulin II (highly expressed in male gametocytes)[43] and HA tag. δ-Tub was expressed specifically in male gametocytes (Fig. 3B). Next, we investigated the subcellular localization dynamic of δ-Tub during male gametogenesis. Before activation, δ-Tub was dispersed in the cytoplasm of the *δ-tub::6HA* male gametocytes. At 1 mpa, δ-Tub started to overlap with the α-Tubulin-labeled tetrad foci (bipartite MTOC) close to the nucleus. From 2 to 8 mpa, the bipartite MTOCs underwent duplication and separation, forming 8 discrete bipartite MTOC foci with which δ-Tub kept associating (Fig. 3C). From 9 mpa, the assembled axonemes and the separated haploid nucleus exflagellate outward together for male gamete release. δ-Tub was localized at the outward end of per flagellated axoneme (Fig. 3C). The localization dynamic of δ-Tub coincided with that of BB in male gametogenesis[10,21], indicating δ-Tub localization at BB. We used U-ExM to further confirm the localization of δ-Tub in BB. Under high resolution, δ-Tub displayed a toroid shape at the proximal end of the axoneme throughout male gametogenesis of the *δ-tub::6HA* parasites (Fig. 3D).

We generated another parasite line *δ-tub::4Myc*, in which δ-Tub was endogenously tagged with a 4Myc epitope in 17XNL. We stained the *δ-tub::4Myc* gametocytes with antibodies against Myc and PolyE. *δ-tub::4Myc* displayed similar localization dynamics at BB during male gametogenesis as *δ-tub::6HA* (Supplementary Fig. 6D, E).

δ-Tub and ε-Tub are essential for male gametogenesis and mosquito transmission of parasites

To elucidate the function of δ-Tub and ε-Tub in the parasite, we deleted the coding sequence of *δ-tub* (2064 bp) and *ε-tub* (1503 bp), respectively in the 17XNL parasite using CRISPR-Cas9 (Fig. 4A), generating two mutant clones *Δδ-tub* and *Δε-tub*. Both mutants showed normal development of asexual blood stages and gametocytes in mice (Fig. 4B, C). We measured the in vitro female gametogenesis by analyzing P28 expression in activated female gametocytes. Gene deletion of *δ-tub* or *ε-tub* had no impact on female gamete formation (Fig. 4D). We measured male gametogenesis by counting exflagellation centers (ECs)

https://doi.org/10.1038/s41467-025-64158-8

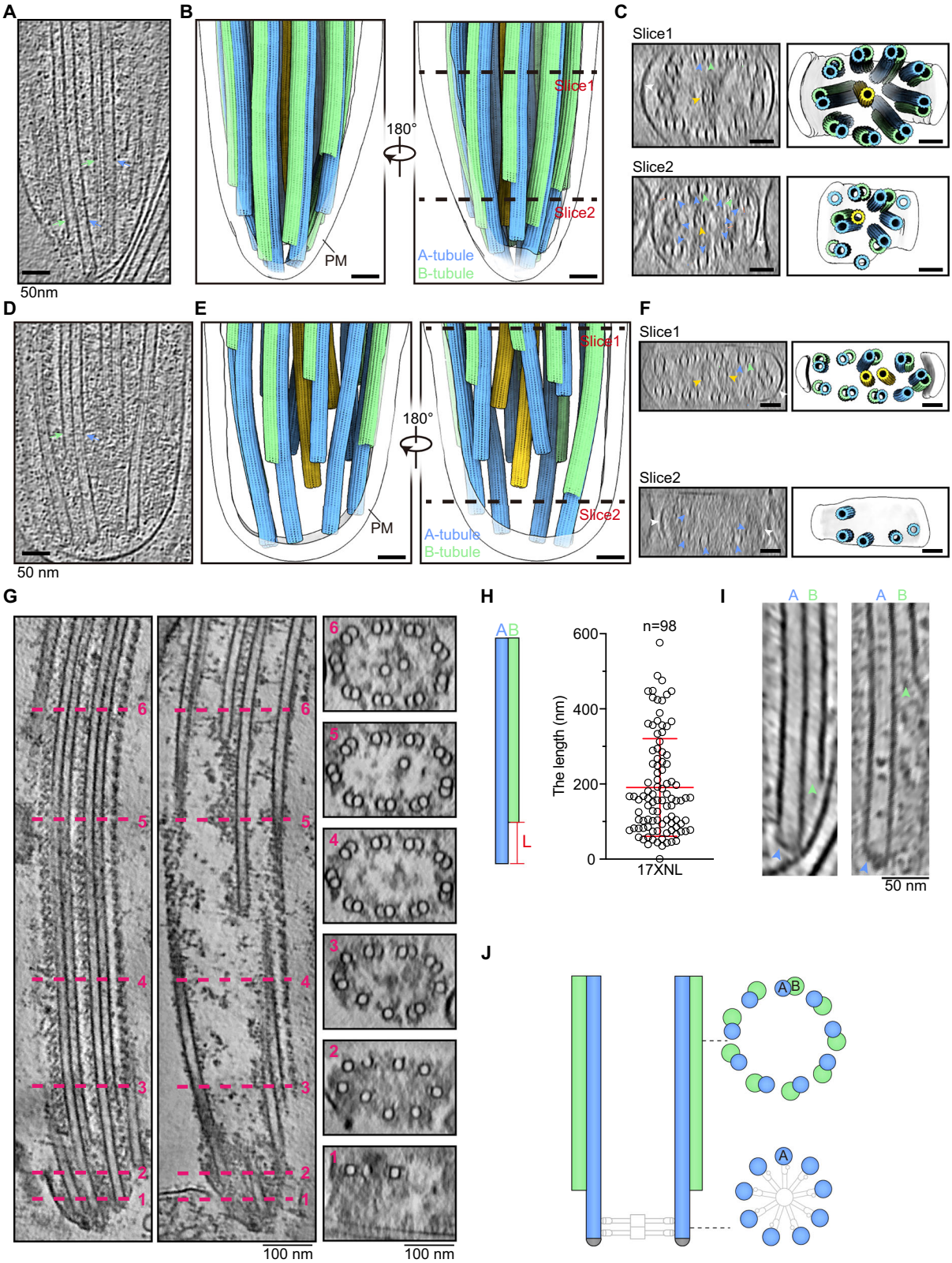

in vitro after stimulating with 50 µM xanthurenic acid (XA) at 22 °C. Both *Δδ-tub* and *Δε-tub* showed a complete deficiency in the ECs formation (Fig. 4E and G) and male gamete release (Fig. 4F and H). Without fertile male gamete, the *Δδ-tub* and *Δε-tub* parasites failed to develop the ookinetes in vitro (Fig. 4I). To evaluate the transmission ability of mutant parasites in the mosquito, parasite-infected mice were fed to the *Anopheles stephensi* mosquitoes. Both *Δδ-tub* and *Δε-tub* produced no midgut oocysts (Fig. 4J) and no salivary gland sporozoites (Fig. 4K), indicating failure of parasite transmission in the mosquitoes.

We genetically complemented the mutant parasites to confirm the defective phenotype caused by *δ-tub* or *ε-tub* gene deletion. The deleted 2064 bp sequence of *δ-tub* fused with a 4Myc was introduced back to the *δ-tub* locus of Δ*δ-tub*, obtaining the complemented parasite line *comp1* (Fig. 4A), while the deleted 1503 bp sequence of *ε-tub*

Fig. 2 | Cryo-electron tomography (Cryo-ET) of MT singlet-to-doublet transition. A A 0.9 nm thick tomographic slice exhibits the proximal part of the male gamete in the *P. yoelii* 17XNL parasite. The A-tubule (blue) and B-tubule (green) of MT doublet were indicated by arrows. A representative from two independent experiments. Scale bars = 50 nm. **B** 3D rendering of tomograms for the male gamete in (**A**). MT doublet's A-tubule (blue) and B-tubule (green) are colored. A central pair of MT singlets (yellow) and the parasite plasma membrane (PM) was denoted. Scale bars = 50 nm. **C** Cross-section view (left) and 3D rendering (right) of MTs in axoneme (slice 1) and basal body (slice 2) from (**B**). A representative from two independent experiments. Scale bars = 50 nm. A-tubule (blue), B-tubule (green), and parasite plasma membrane (white) were indicated by arrowheads. **D**–**F** A 0.9 nm thick tomographic slices and 3D rendering of tomogram showing the proximal part of another male gamete. A representative from two independent experiments. **G** Vertical-section and cross-section views of a Cryo-ET tomogram showing the MT singlet-to-doublet transition in the BB of the male gamete. In the left panels, two slices from the same tomogram were shown, with each slice being 2 nm thick. Six slices (pink dash lines positioned in the cross sections) were shown in the right panels. A representative from two independent experiments. Scale bars = 100 nm. **H** Quantification of the distance between the proximal end of A-tubule and B-tubule in the MT doublet. Left panel is a schematic showing the distance measured. Mean ± SD for the MT doublets ($n = 98$) measured from two independent experiments, two-tailed t-test. **I** Vertical-section view showing the proximal end of the A-tubule (blue arrowhead) and B-tubule (green arrowhead) in the MT doublets from two different Cryo-ET tomograms. A representative from two independent experiments. Scale bars = 50 nm. **J** A schematic of the MT singlet-to-doublet transition in the BB for axonemal MT doublet assembly in the *P. yoelii*. Source data are provided as a Source Data file.

fused with a 4Myc introduced back to the *ε-tub* locus of Δ*ε-tub*, obtaining the complemented parasite line *comp2* (Fig. 4A). The expression of 4Myc-tagged δ-Tub and ε-Tub was detected in gametocytes of the complemented parasites *comp1* and *comp2* using immunoblot or IFA (Fig. 4L–N). The *comp1* and *comp2* restored male gamete formation in vitro (Fig. 4O) and oocyst formation in mosquitoes (Fig. 4P). These results demonstrated that each of δ-Tub and ε-Tub is essential for male gametogenesis and mosquito transmission of parasites.

δ-Tub and ε-Tub regulate axoneme formation

The BB localization of δ-Tub as well as functional essentiality of δ-Tub and ε-Tub in male gamete formation suggest that both proteins are involved in the BB or axoneme assembly. Upon activation, cytosolic α-Tubulin and β-Tubulin polymerize to the BB-nucleated MTs and produce eight axonemes attached to the nuclear envelope. After axoneme assembly, the BB-guided axoneme and nucleus exflagellate outward from the cell body, releasing eight uniflagellate daughter gametes. We stained the mutant parasites with anti-α/β-Tubulin antibodies and Hoechst 33342 to check the axoneme assembly and release in male gametogenesis. At 8 mpa, the axonemes assembled and coiled around the enlarged nucleus in the gametocytes of 17XNL, Δ*δ-tub*, and Δ*ε-tub* (Fig. 5A). However, the axonemes seemed structurally aberrant in Δ*δ-tub* and Δ*ε-tub* (Fig. 5A). By 15 min, the axonemes exflagellated for male gamete release in 17XNL, but not in Δ*δ-tub* and Δ*ε-tub* (Fig. 5B). We further visualized the defects in axoneme structure under high resolution by U-ExM in male gametocytes at 8 mpa. Compared to the compact and bundled organization of MTs for each axoneme in 17XNL, the axonemal MTs appeared non-bundled in Δ*δ-tub* and Δ*ε-tub* (Fig. 5C). The polymerized MTs were formed, but no intact axoneme was assembled in Δ*δ-tub* and Δ*ε-tub*. Therefore, either δ-Tub or ε-Tub is required for the axoneme assembly in male gametogenesis (Fig. 5D).

Besides a ring of nine peripheral MT doublets, the axoneme also comprises a central pair of MT singlets[44]. We analyzed the assembly of central pair MTs in the axoneme formation of the Δ*δ-tub* and Δ*ε-tub* parasites. PF16 is a conserved axonemal protein localizing at the central pair MTs[45]. From the previously tagged *P. yoelii* parasite *PF16::6HA*[33], we deleted the endogenous *δ-tub* and *ε-tub* and obtained two mutant lines *PF16::6HA*;Δ*δ-tub* and *PF16::6HA*;Δ*ε-tub*. Both IFA and U-ExM demonstrated that the absence of either δ-Tub or ε-Tub does not affect the initial assembly of the central pair MTs. However, the orientation and configuration of central pair MTs are abnormal, likely due to a lack of support by the peripheral nine MT doublets (Supplementary Fig. 7A–C).

In the bipartite MTOC during male gametogenesis, the cytoplasmic BB (outer MTOC part) is connected with the nuclear spindle pole (inner MTOC part)[10]. We investigated whether the loss of δ-Tub or ε-Tub additionally affects spindle formation during male gametogenesis. EB1 has been shown specifically localizing at spindle MTs during the *P. yoelii* male gametogenesis[38]. From the previously tagged *P. yoelii* parasite *eb1::6HA*[38], we deleted the endogenous *δ-tub* and *ε-tub* and obtained two mutant lines *eb1::6HA*;Δ*δ-tub* and *eb1::6HA*;Δ*ε-tub*. IFA revealed that the EB1-labeled spindles elongate and separate normally during male gametogenesis in the absence of either δ-Tub or ε-Tub (Supplementary Fig. 8A, B). U-ExM further observed the characteristic umbrella-like array of spindle MTs in the δ-Tub or ε-Tub mutant parasites (Supplementary Fig. 8C, D). These results show that spindle assembly and dynamics do not depend of proper assembly of axonemes.

δ-Tub is likely localized at the B-tubule proximal end of MT doublet in basal body

Next, we investigated the more precise position of δ-Tub within the BB structure. We performed U-ExM to analyze the spatial relation of δ-Tub relative to the known BB proteins. Three BB proteins SAS6, SAS4, and GCP3 were chosen. The cartwheel is the inner core structure for building BB and SAS6 is the cartwheel assembly protein[46]. SAS6 alone polymerizes into the ninefold symmetrical cartwheel possessing a hub and nine radiating spokes[47]. Surrounding the cartwheel, SAS4 links the radiating spoke and the MT triplets, facilitating the formation of the peripheric MTs[48]. We first tested the known spatial relation between SAS6 and SAS4 in BB. A double-tagged line *sas4::6HA;sas6::4Myc* was generated, in which endogenous SAS6 was tagged with 4Myc and SAS4 with 6HA. IFA showed that SAS6 and SAS4 were diffused in the cytoplasm of male gametocytes. After gametocyte activation, SAS6 and SAS4 were concentrated into foci and co-localized with each other (Supplementary Fig. 9A). These results are consistent with previous reports in *P. berghei*[21,49]. Under high resolution by U-ExM, SAS6 and SAS4 were located at the proximal end of the axoneme, overlapping with the NHS dense-stained BB area in male gametocytes at 2 and 5 mpa (Supplementary Fig. 9B, C). Detailed images revealed that a peripheric ring-like signal of SAS4 surrounded the solid circle signal of SAS6 (Supplementary Fig. 9B, C), in agreement with the localization relation between SAS6 and SAS4 in the canonical structural model of BB[50]. These results proved the feasibility of U-ExM based analysis for fine localization of proteins within the BB structure.

To analyze the relation between δ-Tub and SAS6 or SAS4, we tagged the endogenous SAS6 or SAS4 with 4Myc in the *δ-tub::6HA* parasite, generating two double-tagged parasite lines *δ-tub::6HA;sas6::4Myc* and *δ-tub::6HA;sas4::4Myc*. IFA showed that δ-Tub displayed a similar localization dynamic as SAS6 or SAS4 in activated gametocytes (Supplementary Fig. 9D, E). U-ExM distinguished δ-Tub positioning relative to SAS6 and SAS4 in activated male gametocytes of *δ-tub::6HA;sas6::4Myc* and *δ-tub::6HA;sas4::4Myc* parasites. At 2 and 5 mpa, δ-Tub overlapped the NHS dense-stained BB area (Fig. 6A and C, left panels). The NHS-stained axonemes were nucleated from the BBs, enabling recognition of the proximal to distal axis of BB (see the white arrow in lower panels of Fig. 6A and C). From top views, δ-Tub displayed a toroid shape surrounding a smaller solid circle of SAS6 (Fig. 6A, top panel) or surrounding a smaller ring of SAS4 (Fig. 6C, top

https://doi.org/10.1038/s41467-025-64158-8

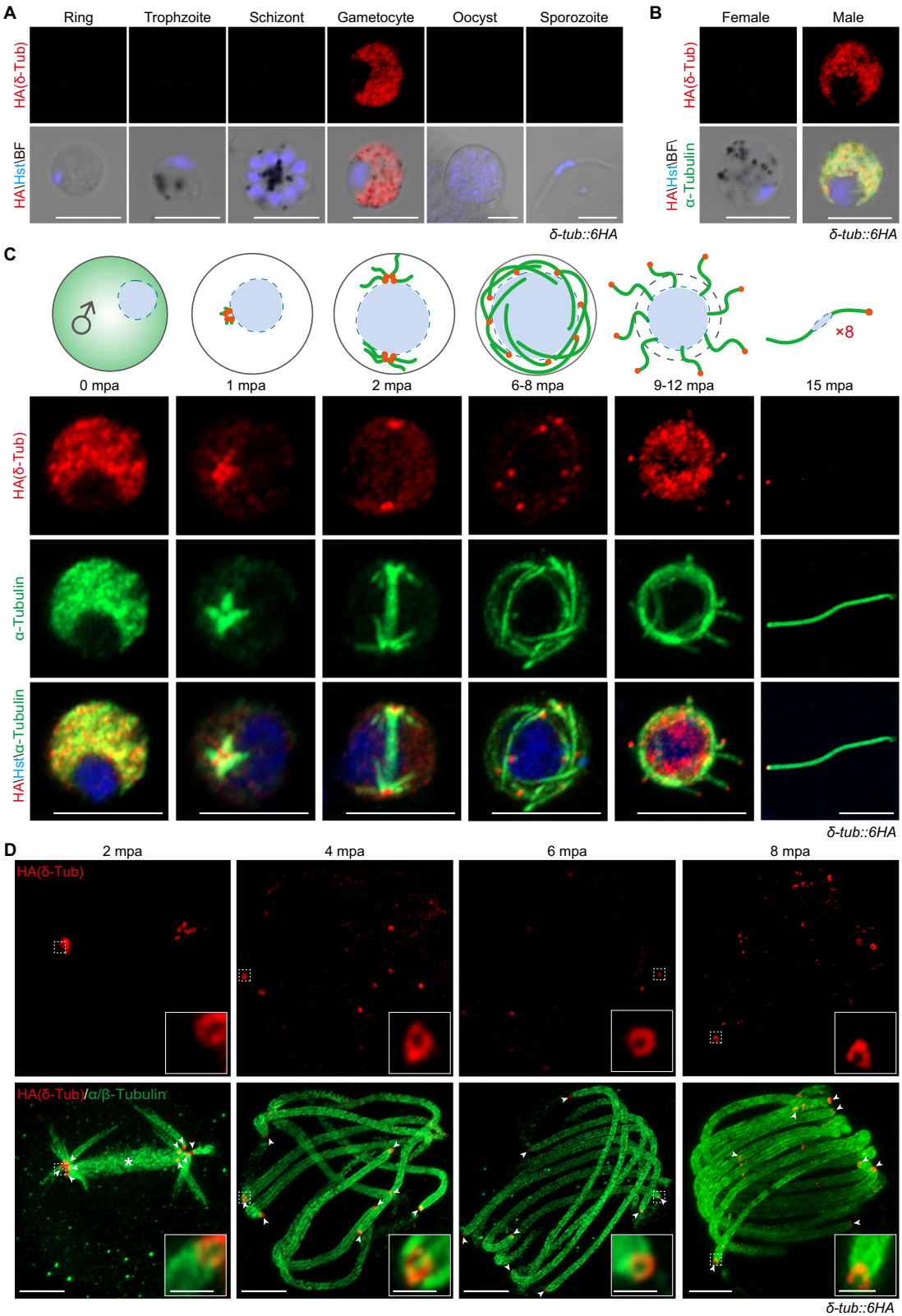

panel), suggesting a peripheral positioning of δ-Tub relative to the inner cartwheel in BB (Fig. 6B and D, top panel). From side views, δ-Tub was located at the distal end of SAS6 (Fig. 6A, lower panel) and SAS4 (Fig. 6C, lower panel), but did not overlay with SAS6 and SAS4. δ-Tub displays a peripheric toroid distally surrounding the cartwheel, suggesting the proximal end localization of δ-Tub at the peripheric MTs of BBs (Fig. 6B and D).

We further clarified the association of δ-Tub with the A- or B-tubule of the peripheric MT doublets in BBs. The γ-TuRC complex nucleates the MT singlet at the minus end[41], and is thought to be located at the proximal end of A-tubules in peripheric MT doublets in BB[41]. To analyze the relation between δ-Tub and γ-TuRC, we attempted to tag the γ-Tubulin (γ-TuRC core component) but failed. Instead, we tagged another component GCP3 (PY17X_0837700) with 4Myc in the

Fig. 3 | δ-Tubulin is localized at the basal body of activated male gametocytes. **A** Immunofluorescence assay (IFA) of δ-Tub expression in different developmental stages of the parasite line *δ-tub::6HA* in which the endogenous δ-Tub was tagged with a 6HA in the C-terminus. The parasites were stained with anti-HA antibody and Hoechst 33342 (Hst). A representative from three independent experiments. Scale bars = 5 μm. **B** Co-staining the *δ-tub::6HA* gametocytes with antibodies against HA tag and αII-Tubulin (highly expressed proteins in male gametocyte). A representative from three independent experiments. Scale bars = 5 μm. **C** IFA of HA-tagged δ-Tub and α-Tubulin expression during the male gametogenesis of the *δ-tub::6HA* parasite. A representative from three independent experiments. Upper panels show the schematic development of male gametogenesis. The basal body (red), the axoneme (green), and the nucleus (blue) were indicated. Scale bars = 5 μm. **D** Ultrastructure expansion microscopy (U-ExM) of δ-Tub and α/β-Tubulin during the male gametogenesis of the *δ-tub::6HA* parasite. White arrowhead refers to the basal bodies and white asterisk refers to the nuclear spindle. A representative from three independent experiments. Scale bars = 5 μm. Insets show enlargements of the boxed areas. Scale bars = 1 μm.

δ-tub::6HA parasite, generating another double-tagged line *δ-tub::6-HA;gcp3::4Myc*. IFA showed that δ-Tub was co-localized with the GCP3 foci close to the nucleus in activated male gametocytes (Supplementary Fig. 9F). U-ExM detected that GCP3 was localized as expected in both BB and spindle pole (Fig. 6E, left panels). GCP3 displayed a toroid-like shape, overlaying with the toroid shape of δ-Tub in BBs from top views (Fig. 6E, top panel). From side views, δ-Tub was located at the distal end of GCP3, with a little signal overlaying with GCP3 (Fig. 6E, lower panel). These imaging results of GCP3 supported A-tubule proximal end positioning of γ-TuRC at the peripheric MT in BB. The localization of δ-Tub relative to SAS6, SAS4, and GCP3 strongly suggest that δ-Tub is localized at the B-tubule proximal end in the MT doublets of BBs (Fig. 6B, D, and F).

δ-Tub and ε-Tub are required for B-tubule assembly of MT doublet

Canonical BB assembly includes three sequential steps[41]: (i) cartwheel assembly, (ii) γ-TuRC-dependent nucleation of A-tubules for peripheric MT assembly, (iii) A-tubule wall-based B-tubule assembly by an unknown nucleation mechanism. We performed in-depth experiments to delineate the step(s) affected by δ-Tub or ε-Tub deficiency. In the activated gametocytes of the double-tagged parasite *eb1::6HA;sas6::4Myc*, the cartwheel marker SAS6 was concentrated on the foci adjoining to the EB1-labeled spindle (Supplementary Fig. 10A, B), indicating cartwheel assembly. Lack of either δ-Tub or ε-Tub did not affect the assembly of SAS6-labeled cartwheel in male gametogenesis (Supplementary Fig. 10A, B). Using SAS4 as another cartwheel marker, we observed similar SAS4 concentrations in the δ-Tub- and ε-Tub-null parasites compared to parent strains (Supplementary Fig. 10C, D). These results demonstrated that the cartwheel assembly of BB requires neither δ-Tub nor ε-Tub. In another double-tagged line *eb1::6HA;gcp3::4Myc*, the γ-TuRC protein GCP3 was concentrated to the spindle-adjoining foci in activated gametocytes, indicating the assembly of γ-TuRC at the BB for nucleating the A-tubule of the peripheric MT doublets (Supplementary Fig. 10E, F). The δ-Tub- or ε-Tub-null parasites displayed similar GCP3 concentration as the parent line (Supplementary Fig. 10E, F), suggesting no requirement of δ-Tub or ε-Tub in the γ-TuRC assembly or positioning at the BB.

Given that δ-Tub is localized at the proximal end of the B-tubule in the MT doublets, we speculated that δ-Tub and ε-Tub are involved in assembling the B-tubule in the MT doublets. To investigate this, we analyzed the assembly of the B-tubule in MT doublets during the biogenesis of BB and axoneme in the male gametogenesis of the δ-Tub- or ε-Tub-null parasites. The male gametocytes at 2 mpa were stained with antibodies against α/β-Tubulin and PolyE, marking the mature B-tubule of MT doublet in male gametogenesis (Supplementary Figs. 2D and 3A). U-ExM revealed that the axonemal and spindle MTs were present in the 17XNL, Δ*δ-tub*, and Δ*ε-tub* parasites (Fig. 7A). Notably, PolyE was detected in the axonemal MTs at the proximal area in 17XNL, but not in Δ*δ-tub* or Δ*ε-tub* (Fig. 7A, B), indicating no or defective assembly of B-tubule. Consistent with the absence of B-tubule for peripheral MT doublet assembly, the diameters of axonemes were smaller in the Δ*δ-tub* (155 ± 10 nm, $n = 40$) and Δ*ε-tub* (151 ± 13 nm, $n = 32$) compared to 17NXL (241 ± 17 nm, $n = 32$) (Fig. 7A and C).

We performed iU-ExM to analyze the B-tubule assembly in the axonemal MT doublets in male gametocytes at 8 mpa. Cross-section images detected the "9 + 2" organization of axonemal MTs in 17XNL, and nine peripheral MT doublets were PolyE positive (Fig. 7D). However, the Δ*δ-tub* or Δ*ε-tub* parasites exhibited non-structured axoneme configuration, with loose α/β-Tubulin signal and significantly reduced polyE signal (Fig. 7D). We also performed TEM to dissect the ultrastructural defects in B-tubule formation of the axonemal MT doublets in male gametocytes at 8 mpa. The 17XNL parasites displayed "9 + 2" MT arrangement of axonemes in most gametocytes (92.7 ± 0.6%, $n = 141$) at 8 mpa (Fig. 7E, F). Loss of either δ-Tub or ε-Tub caused complete loss of "9 + 2" axoneme structure in gametocytes of Δ*δ-tub* (0%, $n = 189$) or Δ*ε-tub* (0%, $n = 183$) (Fig. 7E, F). Compared to the intact A- and B-tubules in the MT doublets of 17XNL (99.7 ± 0.6%, $n = 496$), Δ*δ-tub* or Δ*ε-tub* exhibited defective MT doublets with no B-tubule or incomplete B-tubule (79 ± 10%, $n = 260$ in Δ*δ-tub*) or ε-Tub (89 ± 26%, $n = 185$ in Δ*ε-tub*) (Fig. 7E, G). These U-ExM, iU-ExM, and TEM results demonstrated that δ-Tub and ε-Tub are required for B-tubule assembly in the MT singlet-to-doublet transition (Fig. 7H).

BB localization of δ-Tub requires ε-Tub

The single gene deficiency of *δ-tub* or *ε-tub* exhibited similar phenotypes in the B-tubule formation of axonemal MT doublets during male gametogenesis, prompting us to investigate the relationship between δ-Tub and ε-Tub. Since the expression of ε-Tub is too low to be detected by IFA, we focused solely on analyzing the expression and localization of δ-Tub in the ε-Tub-deficient gametocytes. We deleted the endogenous *ε-tub* gene in the double-tagged line *eb1::6HA;δ-tub::4myc*, generating the mutant line *eb1::6HA;δ-tub::4myc;*Δ*ε-tub*. In the gametocytes, ε-Tub disruption did not affect the expression and cytosolic distribution of δ-Tub in gametocyte at 0 mpa (Fig. 8A, B). However, δ-Tub lost BB localization and dispersed in the cytosol in the absence of ε-Tub in activated male gametocytes (Fig. 8C). The percentage of gametocyte with BB localization of δ-Tub is 91 ± 4% in *eb1::6HA;δ-tub::4myc* and 10 ± 5% in *eb1::6HA;δ-tub::4myc;*Δ*ε-tub*. Consistently, U-ExM revealed that a toroid-like signal of δ-Tub was detected adjoining to the EB1-labeled nuclear spindle in the activated male gametocytes of *eb1::6HA;δ-tub::4myc*, but not in the ε-Tub-null parasite (Fig. 8D). These results demonstrated that the BB localization of δ-Tub requires ε-Tub.

Discussion

The structures of BB and centriole are remarkably conserved across eukaryotes and comprised of MT triplets arranged in a ninefold symmetrical configuration[16]. Except for yeasts and higher plants, most eukaryotes possess the BB and centriole, suggesting their presence in the eukaryotic common ancestor[51]. On the other hand, the BB and centriole are assembled in a multiplicity of contexts, including different cell cycle stages or cellular locations for various functions[52]. The BB nucleates cilia and flagellum while the centriole is an essential component of the centrosome, both thus underlying eukaryotic MT-based motility, cell division, and polarity[53]. The conservation of the structure contrasts with the diversity of assembly contexts and functions, suggesting the diversity for tailored assembly of BB and centriole[51].

https://doi.org/10.1038/s41467-025-64158-8

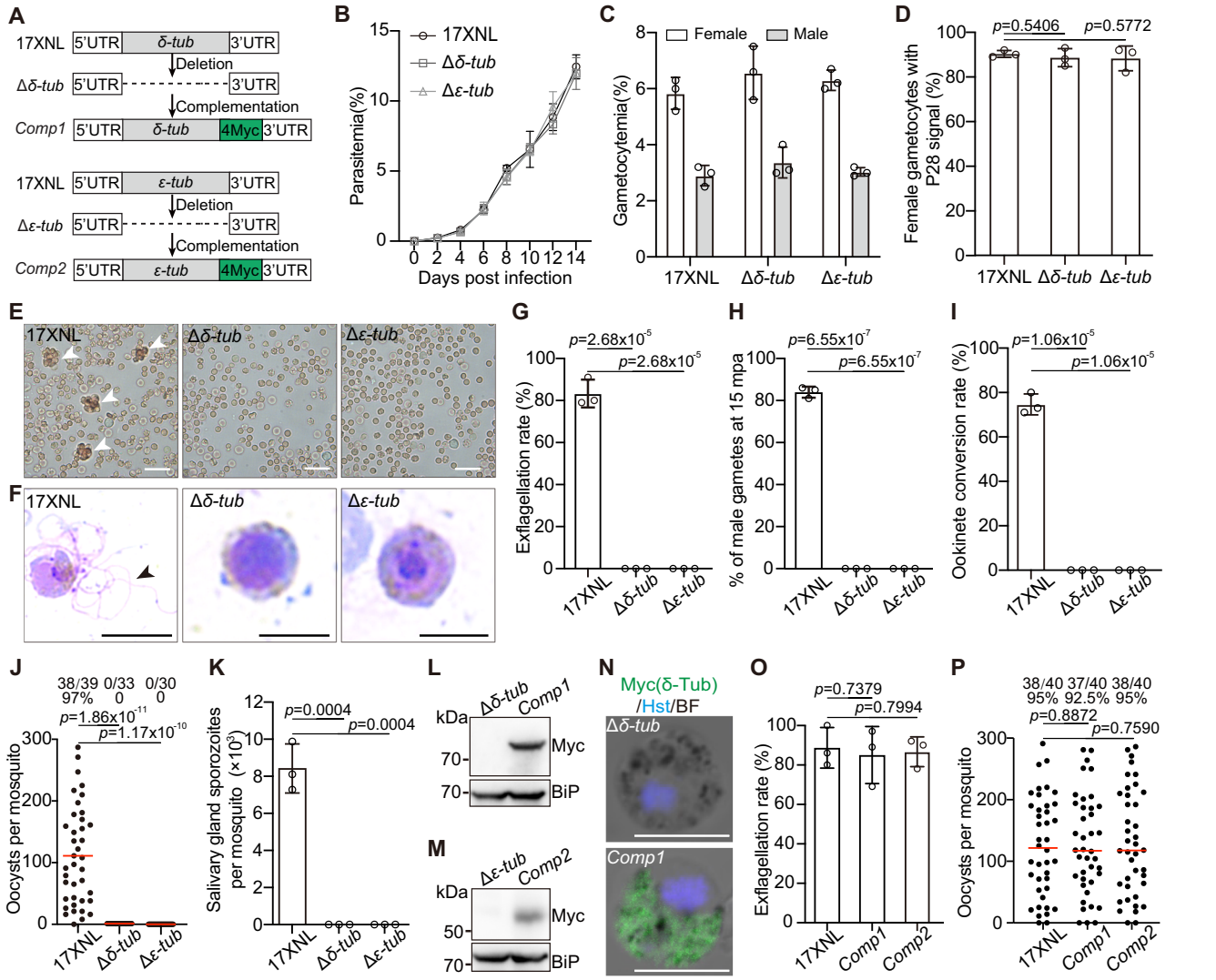

Fig. 4 | δ-Tub and ε-Tub are essential for male gametogenesis and mosquito transmission of parasites. A Schematic showing the gene deletion and complementation in the *P. yoelii* parasite. The coding sequence of *δ-tub* (2064 bp) and *ε-tub* (1503 bp) were deleted respectively in the 17XNL, generating two mutant clones Δ*δ-tub* and Δ*ε-tub*. The *δ-tub* and *ε-tub* gene fused with a 4Myc were introduced back to their locus of the Δ*δ-tub* and Δ*ε-tub,* respectively, generating two complemented lines *Comp1* and *Comp2*. **B** Parasite proliferation at asexual blood stages in mice. Mean ± SD from three mice in each group. A representative from two independent experiments. **C** Male and female gametocyte formation in mice. Mean ± SD from three mice in each group, two-tailed *t*-test. A representative from two independent experiments. **D** In vitro female gamete formation assayed by P28 staining. Mean ± SD for the female gametocytes from three mice in each group, two-tailed *t*-test. **E** In vitro exflagellation assay of male gametocytes. White arrowheads indicate the exflagellation centers of activated male gametocytes. A representative from three independent experiments. Scale bars = 20 μm. **F** Images of the exflagellated male gametes (black arrowhead) after Giemsa staining. A representative from three independent experiments. Scale bars = 5 μm. **G** Quantification of male gametocyte exflagellation in (**E**). Mean ± SD from the infected blood of three mice in each group, two-tailed *t*-test. **H** Quantification of the exflagellated male gametes in (**F**). Mean ± SD from the infected blood of three mice in each group, two-tailed *t*-test. **I** In vitro ookinete formation. Mean ± SD from three independent experiments, two-tailed *t*-test. **J** Midgut oocyst formation in mosquitoes at day 7 post blood feeding. **K** Salivary gland sporozoite formation in mosquitoes at day 14 post blood feeding. 30 infected mosquitoes were counted in each group. Mean ± SD from three independent experiments, two-tailed *t*-test. **L** Immunoblot of δ-Tub in gametocytes of Δ*δ-tub* and *Comp1*. BiP protein as a loading control. A representative from three independent experiments. **M** Immunoblot of ε-Tub in gametocytes of Δ*ε-tub* and *Comp2*. A representative from three independent experiments. **N** IFA of δ-Tub in male gametocytes of Δ*δ-tub* and *Comp1*. A representative from three independent experiments. Scale bars = 5 μm. **O** In vitro exflagellation assay of male gametocytes. Mean ± SD from the infected blood of three mice in each group, two-tailed *t*-test. A representative from three independent experiments. **P** Midgut oocyst formation of parasites in mosquitoes at day 7 post blood feeding. In (**J** and **P**), the red horizontal lines show the median value of oocyst numbers, two-sided Mann–Whitney *U* test. x/y on the top is the number of mosquitoes containing oocyst/the number of mosquitoes dissected; the percentage number is the mosquito infection prevalence. A representative from two independent experiments. Source data are provided as a Source Data file.

One such diverse context is presented by the BB-templated axoneme of the uniflagellate male gamete during mosquito transmission of *Plasmodium*. During *Plasmodium* male gametogenesis, the BB is de novo assembled within a short timeframe, initially tethered at but later decoupled from the nuclear envelope, hence very distinct from canonical BB in biogenesis and dynamics. Given the unique BB cellular contexts for the axonemal assembly, *Plasmodium* may have evolved a novel BB structure. However, the fine structure of MT organization in the BB has not been reported in *Plasmodium* male gametes. In this work, we first applied TEM and iU-ExM to analyze the MT organization in the BB of the activated male gametocytes of *P. yoelii*. We did not detect the existence of canonical MT triplet. Instead, only the MT singlet and doublet were detected in the BB of the activated male gametocytes, confirming the previous observation from *P. berghei*[21].

https://doi.org/10.1038/s41467-025-64158-8

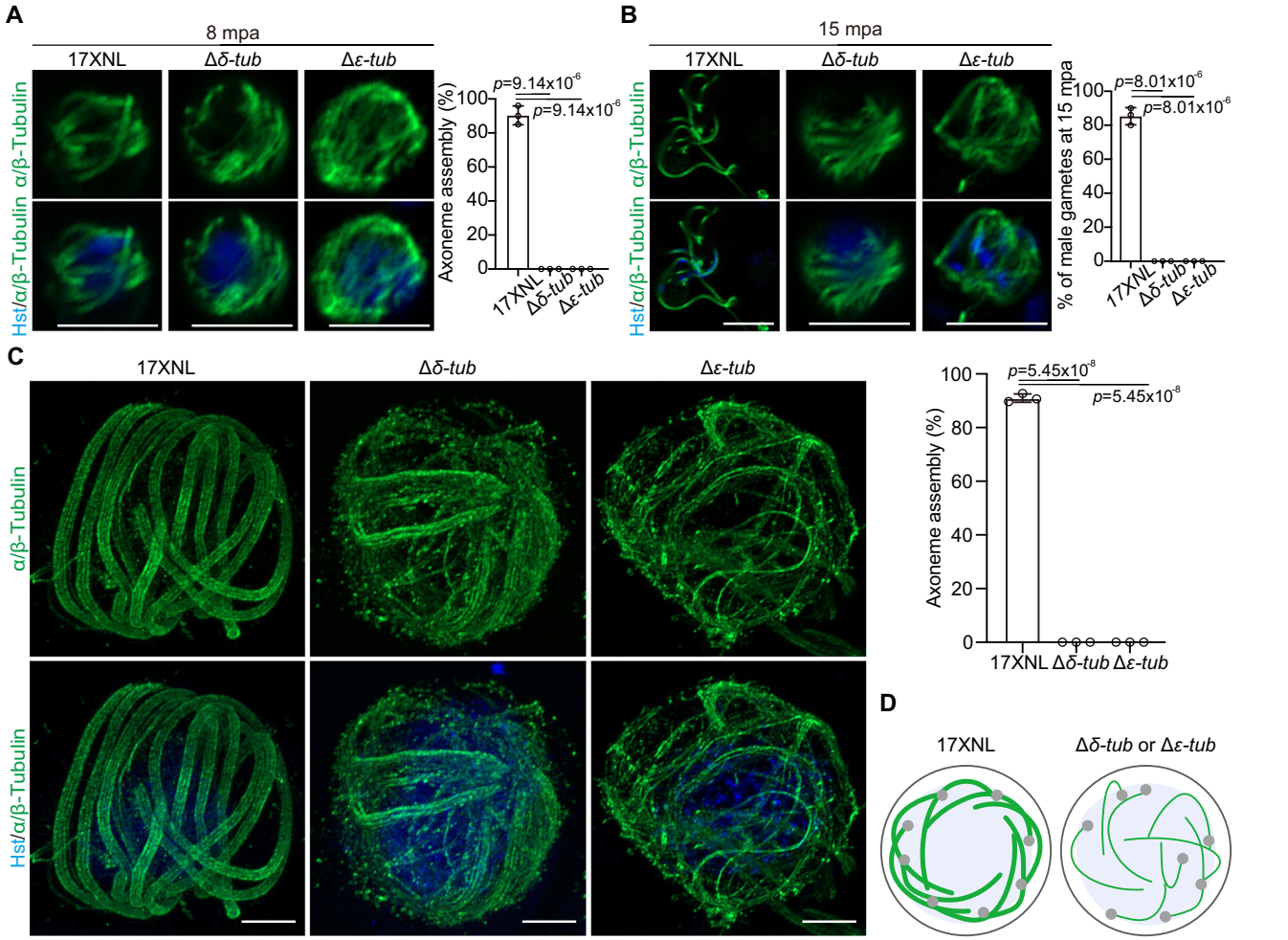

Fig. 5 | δ-Tub and ε-Tub regulate axoneme formation. A IFA detecting the formation of cytoplasmic axonemes in the gametocytes at 8 mpa. Parasites were stained with the α/β-Tubulin antibodies and Hoechst 33342. Scale bars = 5 μm. Right panel is the quantification of male gametocytes with normal axoneme assembly. Mean ± SD from three independent experiments, two-tailed *t*-test. **B** IFA detection of the exflagellated axonemes in the gametocytes at 15 mpa. Scale bars = 5 μm. Right panel is the quantification of male gametocytes with released axoneme. Mean ± SD from three independent experiments, two-tailed *t*-test. **C** U-ExM detection of the cytoplasmic axoneme formation in the gametocytes at 8 mpa. Parasites were stained with the α/β-Tubulin antibodies and Hoechst 33342. Scale bars = 5 μm. Right panel is the quantification of male gametocytes with normal axoneme assembly. Mean ± SD from three independent experiments, two-tailed *t*-test. **D** Cartoon showing the δ-Tub or ε-Tub deficiency in axonemes assembly during male gametogenesis. The basal body (gray), the axoneme (green), and the nucleus (light blue) were indicated. Source data are provided as a Source Data file.

Cryo-ET is a powerful imaging technique that can provide subcellular details of cells in 3D space at nanometer resolution under near-physiological conditions[54]. Recent cryo-ET analyses have revealed the in situ structure and organization of several subcellular structures, organelles, and macromolecules in the *Plasmodium* parasites, including the apical complex in the *P. falciparum* merozoites[55], the rhoptry secretion system in the *P. falciparum* merozoites[56], and the variable microtubule cytoskeleton of *P. falciparum*[57]. In this study, we performed cryo-ET to resolve the native MT structure and organization in the BB of *P. yoelii* male gametes. A continuous transition from MT singlet to MT doublet was visualized in the BB of male gametes. This MT singlet-to-doublet transition pattern differs from the MT triplet-to-doublet transition in canonical axonemal MT formation. We proposed a model for this MT singlet-to-doublet transition in Fig. 8E. In addition, the MT singlet-to-doublet transition is heterogeneous in the BB of male gametes, distinct from the homogenous MT triplet-to-doublet transition in the canonical BB. Therefore, *Plasmodium* evolved a unique but seemingly simplified MT organization of BB for axonemal MT doublet assembly. Our study provides new insights into the diversity of MT organizations in the BB assembly.

What is the potential benefit of BB with the MT singlet-to-doublet transition in the *Plasmodium*? In *Plasmodium* male gametogenesis, the BB is de novo assembled, tethered at the nuclear envelope, and coupled with the nuclear spindle pole in the bipartite MTOC[10]. After the assembly of eight axonemes, all eight BBs need to undergo decoupling from the nuclear envelope for axoneme exflagellation. It is reasonable that the MT singlets may likely be less stabilized than the MT triplet in supporting the cytoskeleton-based structure. From this perspective, the BB with MT singlet organization rather than MT triplet may be more structurally flexible and be more conducive to the coupling and decoupling dynamics during the extraordinarily rapid male gametogenesis.

The cartwheel structure in the canonical BB or centriole serves as a central hub from which nine spoke structures extend radially[58]. The cartwheel and spokes play a vital role in organizing the MT triplets, enabling the nine MT triplets to form a circular pattern[59]. Unexpectedly, the signals corresponding to the structures of the cartwheel and spokes were not detected in BB's TEM and cryo-ET imaging in the *Plasmodium* (Figs. 1H and 2G). It is possible that after the assembly of the axoneme, the cartwheel structure of the BB becomes unstable or

https://doi.org/10.1038/s41467-025-64158-8

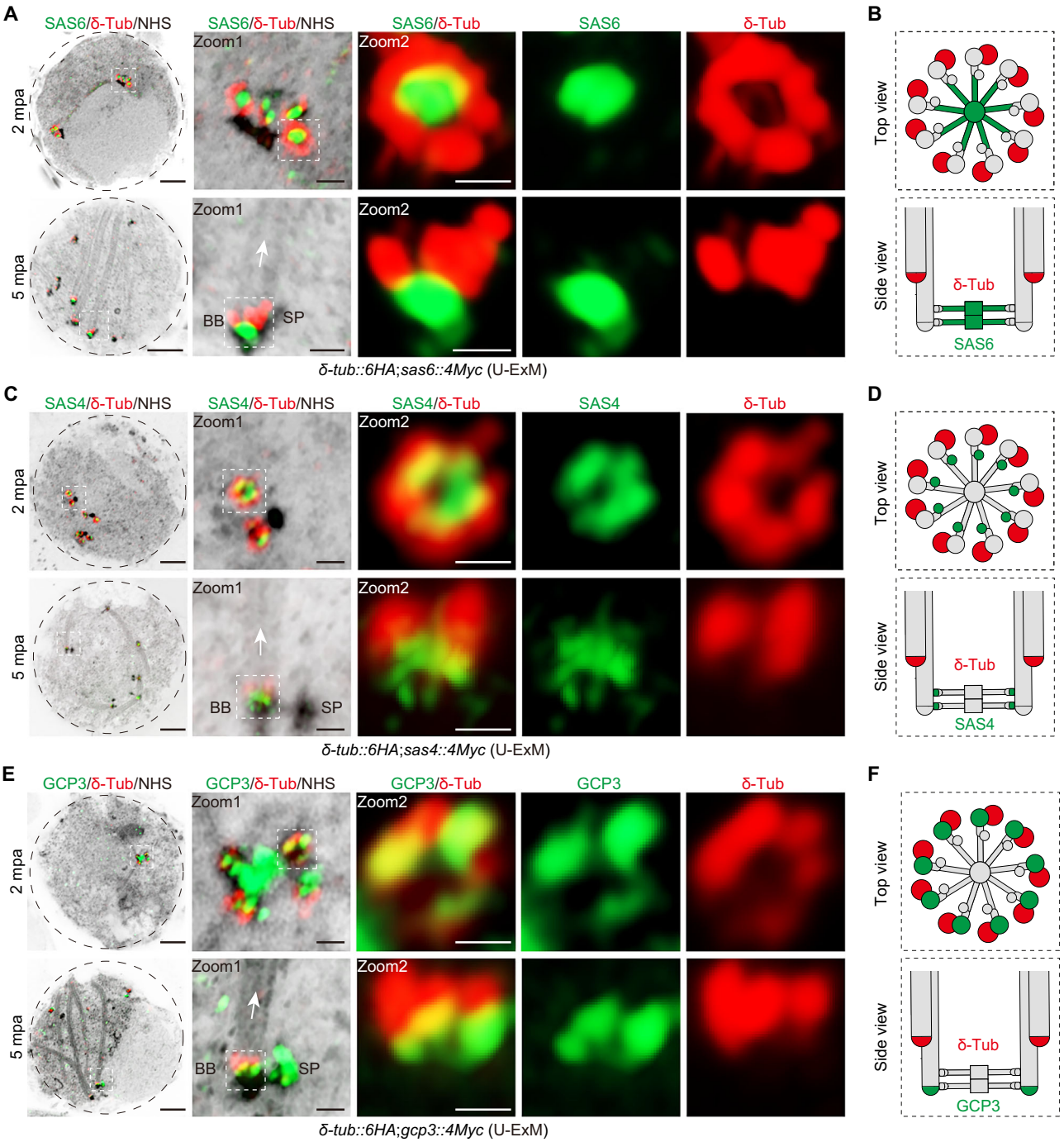

Fig. 6 | δ-Tub is localized at the proximal end of the B-tubule of MT doublet. **A** U-ExM of δ-Tub and SAS6 in male gametocytes of the double-tagged line *δ-tub::6HA;sas6::4Myc* at 2 mpa (top panel) and 5 mpa (lower panel). SAS6 is a cartwheel protein of the basal body. Parasites were stained with NHS-ester dye and antibodies against HA and Myc. The basal body and axoneme were labeled with the NHS-ester dye. A white arrow indicates the proximal-to-distal direction of the axoneme. Scale bars = 5 µm. Insets (Zoom1) show enlargements of the boxed areas. Scale bars = 1 µm. Insets (Zoom2) show enlargements of the boxed areas in Zoom1. Scale bars = 500 nm. A representative from three independent experiments. **B** Localization schematic of δ-Tub (red) and SAS6 (green) in the basal body from (**A**). **C** U-ExM of δ-Tub and SAS4 in male gametocytes of the double-tagged line *δ-tub::6HA;sas4::4Myc* at 2 and 5 mpa. SAS4 is another cartwheel protein in the basal body. Parasites were stained with NHS-ester dye and antibodies against HA and Myc. A white arrow indicates the proximal-to-distal direction of the axoneme. Scale bars = 5 µm. Insets (Zoom1) show enlargements of the boxed areas. Scale bars = 1 µm in Zoom1 insets. Scale bars = 500 nm in Zoom2 insets. A representative from three independent experiments. **D** Localization schematic of δ-Tub (red) and SAS4 (green) in the basal body from (**C**). **E** U-ExM of δ-Tub and GCP3 in male gametocytes of the double-tagged line *δ-tub::6HA;gcp3::4Myc* at 2 and 5 mpa. GCP3 is a subunit of γ-TuRC positioning at the proximal end of A tubule in MT doublet. A white arrow indicates the proximal-to-distal direction of the axoneme. Scale bars = 5 µm. Insets (Zoom1) show enlargements of the boxed areas. Scale bars = 1 µm in Zoom1 insets. Scale bars = 500 nm in Zoom2 insets. A representative from three independent experiments. **F** Localization schematic of δ-Tub (red) and GCP3 (green) in the basal body from (**E**).

https://doi.org/10.1038/s41467-025-64158-8

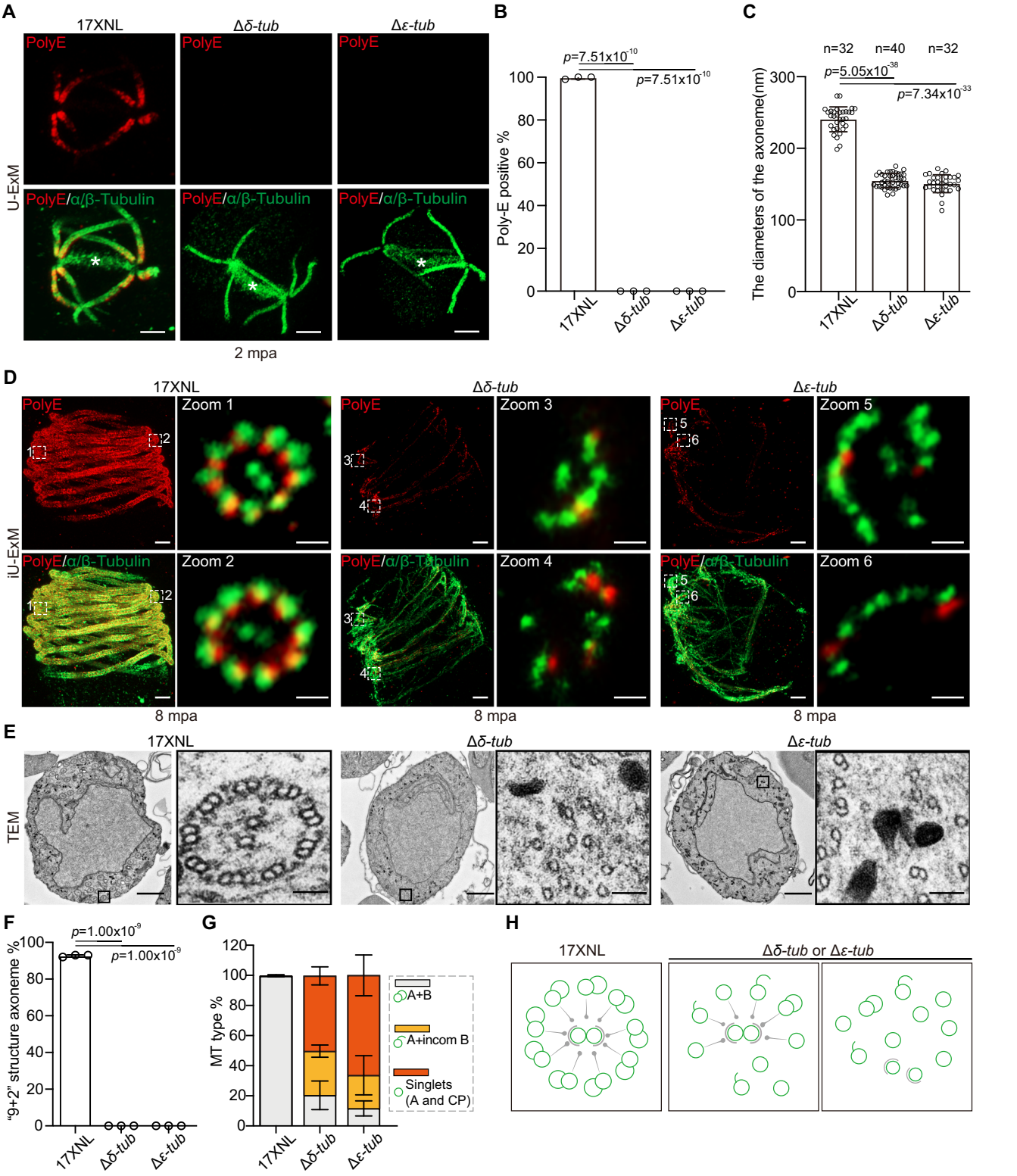

disassembles. Similar to this observation, the cartwheel structure disassembles after the assembly and maturation of human centrioles[60]. Another possibility is that *Plasmodium* may have a simpler cartwheel structure despite the presence of essential factors for cartwheel assembly, including SAS6 and SAS4. Consistent with it, comparative genomic analysis detected fewer conserved BB components, including the cartwheel or radial spoke proteins, in the *Plasmodium*[61].

In eukaryotes, MT exists in three structural forms: singlet (A tubule), doublet (A-B tubules), and triplet (A-B-C tubules)[62]. The A tubule consists of 13 protofilaments, while the B and C tubules are incomplete, each containing 10 protofilaments. MT singlets are distributed throughout the cytoplasm of eukaryotic cells; MT doublets are found in the axonemes of cilia and flagella; and MT triplets are present in BBs and centrioles. The A tubule MT is nucleated by the multi-subunit complex γ-TuRC, which provides an assembly template for the 13 protofilaments arranged in a cylindrical shape[63]. It has been established that MT doublets and triplets are structurally derived from MT singlets. However, the MT singlet-based nucleation and assembly

Fig. 7 | δ-Tub and ε-Tub are required for the B-tubule assembly of MT doublet. **A** U-ExM detection of the B tubule formation of MT doublet in the basal body and axoneme of gametocytes at 2 mpa. Parasites were co-stained with antibodies against PolyE and α/β-Tubulin. PolyE marks the mature B-tubule of MT doublet. White asterisk refers to the nuclear spindle. Scale bars = 5 μm. A representative from three independent experiments. The expansion factor is 4 ± 0.3. **B** Quantification of male gametocytes with PolyE labeled axonemal MTs in (**A**). Mean ± SD from three independent experiments, two-tailed *t*-test. **C** Diameter of axoneme in (**A**). *n* is the number of axonemes measured from three independent experiments. Mean ± SD, two-tailed *t*-test. **D** iU-ExM detection of the B tubule formation of MT doublet in the axoneme of gametocytes at 8 mpa. Parasites were co-stained with antibodies against PolyE and α/β-Tubulin. Scale bars = 5 μm. Insets show enlargements of the boxed areas with a cross-section view of the axoneme. Scale bars = 1 μm. A representative from three independent experiments. **E** TEM of axonemal MT architecture in the gametocytes at 8 mpa. Scale bars = 1 μm. Insets show enlargements of the boxed areas with a cross-section view of the axoneme. Scale bars = 100 nm. A representative from three independent experiments. **F** Quantification of male gametocytes with normal "9 + 2" MT structure axoneme. Mean ± SD from three independent experiments, two-tailed *t*-test. **G** Percentage of three types of MT structure in (**E**). Intact MT doublet (A + B tubule), incomplete MT doublet (A tubule + incomplete B tubule), and MT singlet (A-tubule or Central pair (CP) MT singlet). Mean ± SD from three independent experiments. **H** Cartoon showing the δ-Tub or ε-Tub deficiency in the B-tubule formation of MT doublet in the basal body. Source data are provided as a Source Data file.

of MT doublets and triplets remained poorly understood. δ-Tub and ε-Tub have been reported to be localizing in BB or centriole[26,27], and involved in the assembly of MT doublet and triplet[24,25]. However, the precise position of δ-Tub and ε-Tub within BB or centriole and the specific function of δ-Tub and ε-Tub in the assembly of MT doublet and triplet remained elusive. In this study, we revealed that δ-Tub is localized in the BB of activated male gametocytes in the *P. yoelii*, similar to δ-Tub and ε-Tub in other organisms[26,27]. Using the high-resolution imaging method U-ExM and iU-ExM, we further observed that δ-Tub is localized at the proximal end of the B-tubule in the MT doublet at BB. To our knowledge, this is the first report on the precise position of δ-Tub relative to MT doublet in the BB and hence validates the importance of investigating non-model organisms for basic biology function. Consistent with the position of δ-Tub, the loss of δ-Tub specifically impedes the B-tubule assembly of the MT doublet (see the proposed model in Fig. 8E).

How do δ-Tub and ε-Tub function in the assembly of B tubule in the MT doublet in *Plasmodium*? δ-Tub and ε-Tub may contribute to the assembly of the B tubule by two possible mechanisms. One is that δ-Tub and ε-Tub nucleate the initial assembly of the B tubule. The other is that δ-Tub and ε-Tub regulate the stability of the B tubule upon its assembly. In the first mechanism, δ-Tub and ε-Tub act together at the proximal end of the B tubule to nucleate the assembly of the B tubule, similar to the role of γ-TuRC in initiating the assembly of the A tubule. In the cryo-ET images, we observed the cap-like structure, likely the complex of γ-TuRC, at the proximal end of the A tubule of MT doublets in the BB of *Plasmodium* male gametes (Fig. 2I). However, no cap-like structure was observed at the minus end of the B tubule (Fig. 2I). In the second mechanism, δ-Tub and ε-Tub may act together at the proximal end of the B tubule and stabilize the structure of the B tubule upon the initial assembly. During the biogenesis of the human centriole, the A tubule acts as a template for B-tubule assembly that further supports C-tubule growth. The B- and C-tubules elongate bidirectionally from the wall of the A tubule at the proximal end[41]. Previous studies found that the removal of the C-terminal tail of α/β-Tubulin in the A tubule facilitates the formation of MT doublets in vitro[64], suggesting a repressive role of the C-terminal tail of α/β-Tubulin in the A tubule on the B tubule formation. Consistent with this speculation, over-expression of HYLS1 protein, a centriolar protein essential for cilia formation, has been reported to promote the formation of the B tubule, likely by binding to the C-terminal tail of β-Tubulin[65]. In this scenario, δ-Tub and ε-Tub likely bind to the C-terminal tail of α/β-Tubulin on the A tubule and regulate the initial assembly of B tubules in the *Plasmodium*. δ-Tub and ε-Tub may form a complex to regulate the assembly of the B tubule, but the precise composition and interaction within the complex is unknown. In this study, we also demonstrate that δ-Tub lost the BB localization in the absence of ε-Tub. ε-Tub likely interacts with δ-Tub and directly regulates the localization of δ-Tub. Alternatively, ε-Tub may recruit or stabilize an essential partner protein that, in turn, facilitates δ-Tub localization. In addition, the molecular basis of the potential interaction of δ-Tub and ε-Tub with A-tubule wall lattice is also unknown. To understand the key mechanism of δ-Tub and ε-Tub-mediated B tubule assembly, future studies into an atomic resolution structure of the complex composed of δ-Tub and ε-Tub will be required.

Compared to the MT triplet-to-doublet transition commonly seen, the male gamete of *Plasmodium* possesses the MT singlet-to-doublet transition pattern, providing a simple in vivo model for investigating the MT doublet assembly. Our study establishes a more precise localization and function understanding of δ-Tub and ε-Tub on the MT doublet assembly. In the future, it will be critical to further elucidate the potential nucleating or modulating role of δ-Tub and ε-Tub in the B tubule assembly during the MT singlet-to-doublet transition in the *Plasmodium*.

Methods

Mice and mosquitoes usage and ethics statement

The animal experiments conducted in this study were approved by the Committee for Care and Use of Laboratory Animals of Xiamen University (XMULAC20230333). Female ICR mice aged 5–6 weeks were acquired from the Animal Care Center of Xiamen University. The mice were housed in a controlled environment at 22–24 °C, with a relative humidity of 45–65% and a 12 h light/dark cycle. They were used for parasite propagation, drug selection, parasite cloning, and mosquito feeding. The rodent malaria parasite *P. yoelii* 17XNL strain is propagated in ICR mice. For parasite passage, appropriate 1.0×10^5 parasite-infected erythrocytes were administered to the naïve mice via tail vein injection. The larvae of *Anopheles stephensi* mosquitoes (*Hor* strain) were maintained in an insect facility under controlled conditions of 28 °C, 80% relative humidity, and a 12 h light/dark cycle. Adult mosquitoes were fed with a 10% (w/v) sucrose solution containing 0.05% 4-aminobenzoic acid and kept at 23 °C.

Chlamydomonas reinhardtii culture. The *C. reinhardtii* strain (CCMA-1031) is provided by the Center for Collections of Marine Algae (The State Key Laboratory of Marine Environmental Science, Xiamen University). Cells were cultured on 1.5% agar plates or in liquid Tris-acetate-phosphate medium at 23 °C with slow shaking under 14/10 h light/dark cycle. The cells were sedimented on 15 mm Poly-D-Lysine coated coverslips for 10 min, after which the excess was removed, and the cells were fixed with cold methanol for 7 min.

Plasmid construction and parasite transfection

The CRISPR/Cas9 plasmid pYCm was used for parasite genomic modification[42]. To construct plasmid vectors for gene editing, we amplified 5′ and 3′ genomic sequence (300–800 bp) of target genes as homologous arms using specific primers (Supplementary Table 1) and inserted the sequences into specific restriction sites in pYCm. Oligonucleotides for guide RNAs (sgRNAs) (Supplementary Table 1) were mixed in pairs, denatured at 95 °C for 3 min, annealed at room temperature for 5 min, and ligated into pYCm. The sgRNAs were designed to target the coding region of a gene (Supplementary Table 1) using the online website PlasmoDB database. DNA fragments encoding 6HA or 4Myc tags were inserted between the left and right arms in frame with

https://doi.org/10.1038/s41467-025-64158-8

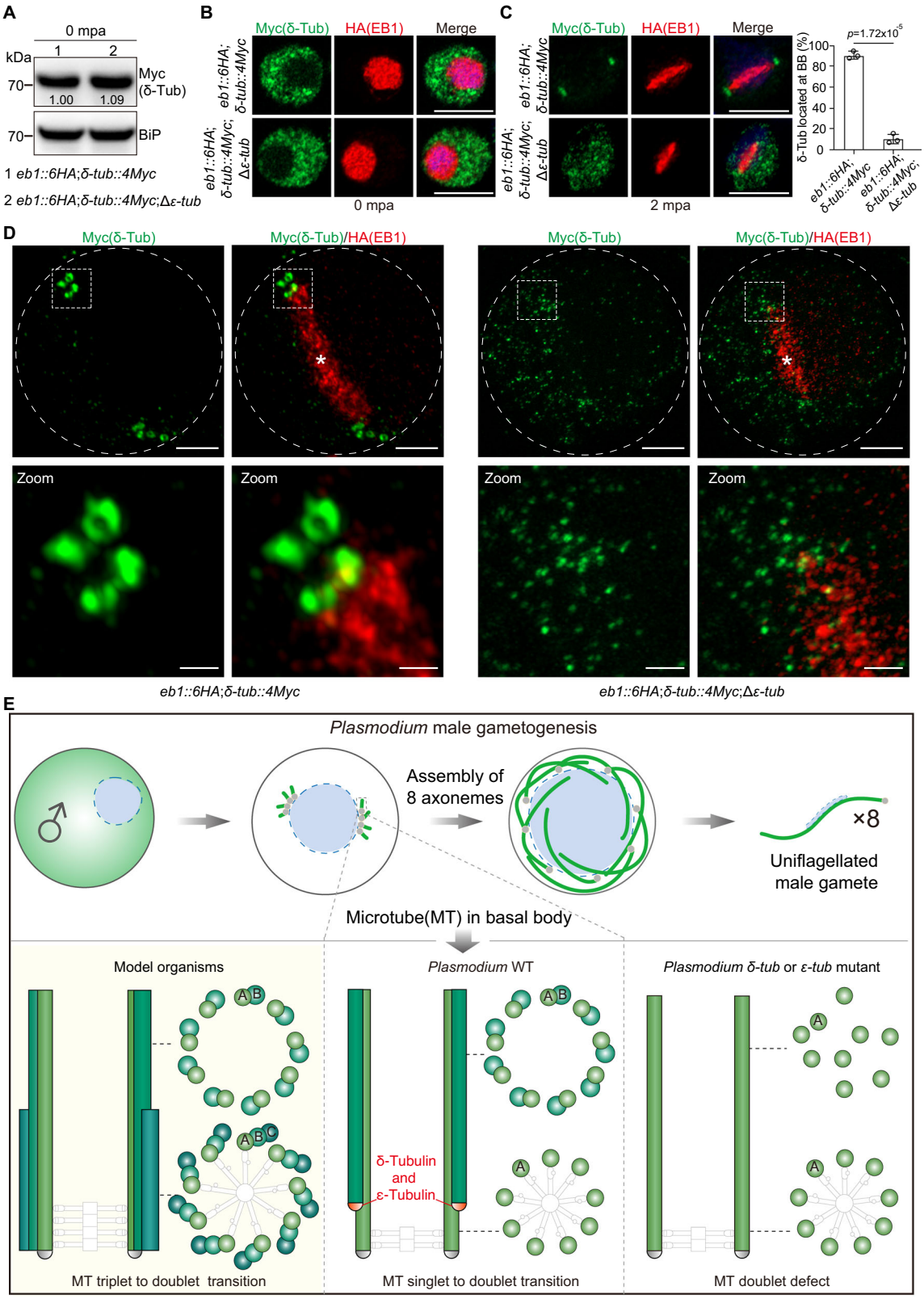

gene of interest. For each gene, at least two sgRNAs were designed to target sites close to the C- or N-terminal regions. Infected red blood cells were electroporated with 5 μg plasmid using a Nucleofector 2b Device (Lonza, Germany). Transfected parasites were immediately intravenously injected into a naive mouse and exposed to pyrimethamine (7.0 mg/mL) 24 h post-transfection. Parasites with transfected plasmids typically appeared after 5–7 days under drug pressure. Single clones of parasite were obtained by limiting dilution in mice, and genomic DNA was extracted from infected mouse blood for PCR genotyping using specific primers listed in Supplementary Table 1. PCR genotyping results of single cloned parasites were presented in Supplementary Fig. 11. Modified parasites subjected to sequential modification were negatively selected to remove pYCm plasmid. 5-Fluorouracil (5-FC, Sigma-Aldrich, F6627) was prepared in water

Fig. 8 | Basal body localization of δ-Tub requires ε-Tub. A Immunoblot of δ-Tub in gametocytes of the *eb1::6HA;δ-tub::4Myc* and *eb1::6HA;δ-tub::4Myc;Δε-tub* parasite lines. BiP as a loading control. The numbers show the signal level of δ-Tub after normalizing with that of BiP. A representative from two independent experiments. **B** IFA of δ-Tub in gametocytes of the *eb1::6HA;δ-tub::4Myc* and *eb1::6HA;δ-tub::4-Myc;Δε-tub* parasite lines. Parasites were stained with antibodies against HA and Myc. EB1 is a nuclear spindle protein. A representative from three independent experiments. Scale bars = 5 μm. **C** IFA of δ-Tub in gametocytes at 2 mpa. Scale bars = 5 μm. Right panel shows the percentage of gametocytes with δ-Tub localizing at the basal body. Mean ± SD from three independent experiments, two-tailed *t*-test. **D** U-ExM detection of δ-Tub in gametocytes at 2 mpa. Scale bars = 5 μm. Insets show enlargements of the boxed areas. White asterisk refers to the nuclear spindle. Scale bars = 1 μm. A representative from three independent experiments. **E** A proposed model for the basal body MT singlet-to-doublet transition during male gametogenesis of *P. yoelii* and the contribution of δ-Tub and ε-Tub in the MT B-tubule assembly for axonemal MT doublet formation. Source data are provided as a Source Data file.

(2.0 mg/mL) and provided to the mice in drinking water in a dark bottle. Naive mice receiving parasites with residual plasmids after pyrimethamine selection were subjected to 5-FC pressure until PCR confirmed plasmid elimination. All the genetically modified parasite lines generated in this study were listed in Supplementary Table 2.

Parasite intraerythrocytic asexual proliferation in mouse

Parasite proliferation rates in the asexual blood stage were determined in mice injected intravenously with 1.0×10^5 parasites. Three ICR mice were included per group. Parasite growth was monitored by Giemsa-stained thin blood smears every two days from day 2 to 14 post-infection. Parasitemia was calculated as the ratio of parasitized erythrocytes to total erythrocytes.

Gametocyte induction in mouse

ICR mice were treated with phenylhydrazine (80 μg/g mouse body weight; Sangon Biotech, China, cat#A600705-0025) via intraperitoneal injection. Three days post-injection, mice were infected with 4.0×10^6 parasites by intravenous injection. Gametocytemia usually peaks at day 3 post-infection. Male and female gametocytes were counted on Giemsa-stained blood smears. Sex-specific gametocytemia was calculated as the ratio of male or female gametocytes to parasitized erythrocytes.

Gametocyte purification

Gametocytes were purified using the method described previously[66]. Briefly, mice were treated with phenylhydrazine 3 days before infection. From day 3 post-infection, sulfadiazine (20 mg/L; Sigma-Aldrich, cat#S8626) was administered in drinking water to eliminate the asexual blood stage parasites. After two days of treatment with sulfadiazine, approximately 1 mL of gametocyte-containing mouse blood was collected from the orbital sinus and suspended in 6 mL gametocyte maintenance buffer (GMB, 137 mM NaCl, 4 mM KCl, 1 mM CaCl2, 20 mM glucose, 20 mM HEPES, 4 mM NaHCO3, 0.1% BSA, and pH 7.2). The 7 mL parasite sample was layered on top of a 2 mL 48% Nycodenz solution (27.6% w/v Nycodenz in 5 mM Tris-HCl, 3 mM KCl, 0.3 mM EDTA, and pH 7.2) in a 15 mL Falcon tube. After centrifugation at 1900 × *g* for 20 min, the gametocytes were collected from the interface layer and washed twice with GMB for further use.

Male gametocyte exflagellation assay in vitro

A 2.5 μL aliquot of mouse tail blood containing 4–10% gametocytemia was added to 100 μL exflagellation medium (RPMI 1640, 100 μM XA [Sigma-Aldrich, cat#D120804], 2 U/mL heparin, pH 7.4). After 10 min of incubation at 22 °C, the exflagellation centers (ECs) and RBCs were counted in a hemocytometer under a light microscope. The percentage of RBCs containing male gametocytes was calculated from Giemsa-stained smears, and the exflagellation rate was calculated as ECs per 100 male gametocytes.

Male gametes purification

Male gamete purification was performed according to the protocol for male gamete purification in *P. berghei*[67]. Purified gametocytes were activated in exflagellation medium for 15 min. The parasites were centrifuged at 550 × *g* for 5 min twice. The extracellular male and female gametes in the supernatant were harvested by centrifuging at 10,000 × *g* for 7 min. The pellet parasites were incubated at room temperature for 10 min, allowing the male gametes to swim into the supernatant. After that, the supernatant was harvested and spun at 12,000 × *g* for 10 min at 4 °C and washed twice in PBS.

In vitro ookinete culture and purification

Mouse blood samples carrying 6–10% gametocytemia were collected and immediately added to ookinete culture medium (RPMI 1640, 25 mM HEPES, 10% fetal calf serum, 100 μM XA, 100 μg/mL streptomycin, 100 U/mL penicillin, pH 8.0). The gametocytes were cultured at 22 °C for 12–15 h to allow gametogenesis, fertilization, and ookinete differentiation. Mature ookinete conversion rate was calculated as the number of crescent-shaped mature ookinete (stage V) over that of total ookinetes (from stage I to V). For mature ookinete purification, the culture was centrifugated at 500 × *g* for 5 min. After that, ookinete pellets were resuspended with 7 mL PBS and transferred on the top of 2 mL of 63% Nycodenz in a 15 mL Falcon tube. After centrifuging at 1000 × *g* for 20 min, the interface layer enriched with ookinetes was collected from the tube. Purified ookinetes were used for further biochemical analysis.

Parasite infection and transmission in mosquito

Thirty female *Anopheles stephensi* mosquitoes in one cage were allowed to feed on one anesthetized mouse carrying 4–10% gametocytemia for 30 min at 22 °C. At day 7 post blood feeding, the mosquito midguts were dissected and stained with 0.1% mercurochrome for oocyst observation. At day 14 post blood feeding, the mosquito salivary glands were dissected. Sporozoites from thirty mosquito salivary glands were collected and counted using a hemocytometer, and the average number of sporozoites per mosquito was calculated.

Antibodies and antiserum

Primary antibodies include: rabbit anti-HA (Cell Signaling Technology, cat#3724S, 1:1000 for immunoblotting IB, 1:1000 for immunofluorescence IF), mouse anti-Myc (Cell Signaling Technology, cat#2276S, 1:1000 for IF, 1:1000 for IB), mouse antibody against both α-Tubulin I and α-Tubulin II (Sigma-Aldrich, cat#T6199, 1:1000 for IF), mouse anti-β-Tubulin (Sigma-Aldrich, cat#T5201, 1:1000 for IF), rabbit anti-Polyglutamate chain (PolyE) (AdipoGen, cat#AG-25B-0030, 1:1000 for IF). Secondary antibodies include: HRP-conjugated goat anti-rabbit IgG (Abcam, cat#ab6721, 1:5000 for IB), HRP-conjugated goat anti-mouse IgG (Abcam, cat#ab6789, 1:5000 for IB), Alexa 555 goat anti-rabbit IgG (Thermo Fisher Scientific, cat#A21428, 1:1000 for IF), Alexa 488 goat anti-mouse IgG (Thermo Fisher Scientific, cat#A11001, 1:1000 for IF). The anti-serum rabbit anti-P28 (1:1000 for IFA) and rabbit anti-BiP (1:1000 for IB) were previously prepared in the laboratory[68].

Immunofluorescence assay

Purified parasites were fixed using 4% paraformaldehyde and transferred to a Poly-L-Lysine (Sigma-Aldrich, cat#A-003-M) coated coverslip in a 24-well plate. Fixed cells were permeabilized with 0.1% Triton ×-100 solution in PBS for 10 min, blocked in 5% BSA solution in PBS for 1 h at room temperature, and incubated with the primary antibodies

diluted in 5% BSA-PBS for 1 h at room temperature. After three washes with PBS, the samples were incubated with fluorescently labeled secondary antibodies in 5% BSA-PBS for 1 h at room temperature. Hoechst 33342 at a 1:5000 dilution in PBS was applied for 15 min at room temperature. Finally, the coverslips were washed, mounted in 90% glycerol, and sealed with nail varnish. All images were acquired on Zeiss LSM 980 confocal microscopes.

Ultrastructure expansion microscopy (U-ExM)

Purified gametocytes were sedimented on a 15 mm round poly-D-lysine coated coverslip for 10 min. The parasites were fixed in 4% paraformaldehyde for 15 min. To add anchors to proteins, coverslips were incubated for 5 h in 1.4% formaldehyde/2% acrylamide at 37 °C. Next, gelation was performed in ammonium persulfate (APS, Sigma-Aldrich, cat#A7460); N,N,N′,N′-Tetramethyl ethylenediamine (TEMED, Sigma-Aldrich, cat#110-18-9); Monomer solution (23% Sodium Acrylate (SA, Sigma-Aldrich, cat#408220); 10% AA; 0.1% N,N′-Methylenebisacrylamide (BIS-AA, Sigma-Aldrich, cat#M7279) in PBS) for 1 h at 37 °C. After polymerization, the coverslips were moved to a 6-well plate with denaturation buffer (200 mM SDS, 200 mM NaCl, 50 mM Tris-HCl, and pH 8.8) for 15 min at room temperature to detach the gels. The gels were denatured in 1.5 mL Eppendorf tubes with denaturation buffer at 95 °C for 90 min, incubated with ddH_2O at room temperature overnight in a 10 cm dish for the first round of expansion. The following day, gel samples were washed in PBS twice for 15 min each to remove excess ddH_2O. Gels were cut into square pieces, incubated with primary antibodies at 37 °C for 3 h, and washed with 0.1% PBS-Tween (PBS-T) for 10 min for three times. Incubation with the secondary antibodies was performed for 3 h at 37 °C followed by washing with 0.1% PBS-T for 10 min for three times. Gels were additionally stained by NHS-ester (Thermo Fisher Scientific, cat#A30000) diluted at 10 µg/mL in PBS for 90 min at room temperature. After that, the gels were washed with 0.1% PBS-T for 10 min for three times and expanded in the bulk ddH_2O overnight at room temperature. After the second round of expansion, gels were cut into square pieces (~ 0.5 cm × 0.5 cm) and mounted by a coverslip in a fixed position for imaging. All images were acquired on Zeiss LSM 980 confocal microscopes. The size of each gel was measured before and after expansion. The expansion factor of each gel was determined by calculating the ratio of gel size.

Iterative ultrastructure expansion microscopy (iU-ExM)

Purified gametocytes were sedimented on a 15 mm round poly-D-lysine coated coverslip for 10 min. The parasites were fixed in 4% paraformaldehyde for 15 min. To add anchors to proteins, the sample on coverslip was incubated in 1.4% FA/2% AA in 1× PBS for 5 h at 37 °C. Gelation was performed in 10%AA, 19%SA, 0.1%DHEBA, 0.25%TEMED/APS in PBS for 1 h at 37 °C. After polymerization, the coverslips were moved to a 6-well plate with denaturation buffer (200 mM SDS; 200 mM NaCl; 50 mM Tris-BASE; pH = 6.8) for 15 min at room temperature to detach the gels. The gels were denatured in 1.5 mL Eppendorf tubes with denaturation buffer at 85 °C for 60 min, incubated with ddH_2O at room temperature overnight in a 12 cm dish for the first round of expansion. The following day, gel samples were washed in PBS twice for 15 min each to remove excess ddH_2O. Gels were cut into square pieces, incubated with both primary and secondary antibodies for 3 h at 37 °C, followed by washing with 0.1% PBS-T for 10 min for three times. The gel was next re-expanded in ddH_2O at room temperature overnight. For the second expansion, there are nine experimental steps: (1) The re-expanded gel was cut into 1.0 cm × 1.0 cm pieces, placed in a 6-well plate on ice, and incubated with activated neutral gel (10% AA; 0.05% DHEBA; 0.1% APS/TEMED in ddH_2O) on ice for 10 min for three times; (2) The gel was put on a microscope slide covered by a 22 × 22 mm coverslip for 1 h at 37 °C; (3) The gel embedded in the neutral gel was incubated in the anchoring solution (1.4% FA/2% AA) for 5 h at 37 °C; (4) The gel was then washed in PBS for 30 min; (5) In a 6-well plate, the gel was washed three times for 10 min under shaking and on ice with the 2nd expansion monomer solution (10% AA, 19% SA, 0.1% BIS, 0.1% TEMED/APS) for $a \pm 16\times$ expansion factor; (6) The excess monomer solution was gently removed and the gel was covered by a 22 × 22 mm coverslip and incubated at 37 °C for 1 h; (7) After the final polymerization, the entire gel was incubated in 200 mM NaOH solution for 1 h under shaking at room temperature followed by washes 20 min with PBS until the pH drops to 7.0; (8) The gel was next dipped in ddH_2O and the water was changed at least three times to ensure the farthest expansion of the gel; (9) After the final expansion, gels were cut into square pieces (0.5 cm × 0.5 cm) and mounted by a coverslip in a fixed position for image acquiring. All images were acquired on Zeiss LSM 980 confocal microscopes. The size of each gel was measured before and after two rounds of expansion. The expansion factor of each gel was determined by calculating the ratio of gel size.

Protein extraction and immunoblot

Parasites were lysed in RIPA buffer (Solaribio, cat#R0010) containing a protease inhibitor cocktail (MedChemExpress, cat#HY-K0010). After ultrasonication, the lysates were incubated on ice for 30 min and centrifuged at 14,000 × *g* for 10 min at 4 °C. The supernatant was mixed with SDS-PAGE loading buffer and heated at 95 °C for 5 min. The extracted proteins were separated in SDS-PAGE, transferred to PVDF membrane (Millipore, cat#IPVH00010), and blocked with 5% milk in TBST (20 mM Tris-HCl pH 7.5, 150 mM NaCl, 0.1% Tween20) at 4 °C overnight. PVDF membranes were then incubated with primary antibodies at room temperature for 1 h. After washing with TBST, the membranes were incubated with an HRP-conjugated secondary antibody and then washed again with TBST. Finally, the membranes were visualized using a high-sensitivity ECL chemiluminescence detection kit (Vazyme, cat#E412-01), and the light emission was recorded by Azure Biosystems C280 (Azure Biosystems, USA).

Transmission electron microscopy

Purified parasites were fixed with 4% glutaraldehyde in 0.1 M phosphate buffer at 4 °C overnight and washed three times with PBS. After that, the parasites were fixed with 1% osmium acid for 2 h and washed three times with PBS. The samples were dehydrated with concentration gradient acetone. After embedding and slicing, thin sections were stained with uranyl acetate and lead citrate. Parasite images were captured by Hitachi HT-7800 electron microscope.

Cryo-ET data acquisition

Gold fiducial beads (6 nm diameter, AURION) were added to the resuspended male gametes in a 1:1 ratio. 4 µL of samples were loaded onto a glow-discharged holey carbon EM grid (Quantifoil R2/1, 200 gold mesh, Jena, Germany) and subsequently vitrified using FEI Vitrobot Mark IV (Thermo Fisher Scientific). The Vitrobot chamber was set to 100% humidity at 22 °C and the vitrified grids were stored in liquid nitrogen before data collection. The parasite samples were imaged in a 300 kV Titan Krios microscope equipped with a Gatan K3 Summit direct electron detector or with a Falcon III direct electron detector, both coupled with a Gatan energy filter (slit width: 20 eV). For Gatan K3 Summit direct electron detector, tilt series were automatically collected using SerialEM[69] with the Plugin PACE-tomo[70] from −60° to +60° in 3° increments and the dose-symmetric tilt scheme was applied[71]. The magnification was set to 26,000 × with the corresponding pixel size of 3.328 Å and the defocus of −3 ~ −5 µm. Images were recorded in a super-resolution mode with 10 frames per image and the accumulated dose was limited to 120 $e^-/Å^2$ of per tilt series. For Falcon III direct electron detector, tilt series were automatically collected using the software Tomography 5 (Thermo Fisher Scientific) from −60° to +60° in 2° increments and the magnification was set to 59,000 × with the

corresponding pixel size of 1.42 Å. Images were recorded in the counted mode with 9 frames per image and the accumulated dose was limited to 130 $e^-/Å^2$ of per tilt series.

Tomogram reconstruction

The MotionCor2[72] motion-corrected tilt images were aligned using patch-tracking or fiducial alignment and reconstructed with back-projection algorithm in IMOD software[73] to obtain tomograms. For visualization and particle picking, the resulting tomograms were rescaled with a binning factor of six, and contrast enhancement was performed with the deconvolution filter in WARP[74].

Segmentation and visualization

The binned tomograms of both datasets were missing-wedge-corrected using IsoNet[75]. Membranes were segmented using MemBrain-Seg (https://github.com/teamtomo/membrain-seg) and manually optimized using Amira (Thermo Fisher Scientific). MT doublets were manually traced in IMOD software[73] and subtomogram volumes were extracted along each MT every 8 nm using the RELION[76] helix toolbox. 3480 subtomogram volumes of MT doublet (2 × binned, 2.84 Å/pixel) were cropped from 9 tomograms in WARP[74] and subtomogram averaging was performed with RELION[76]. The refined results were manually corrected in AriaX[77] and further refined in RELION[76]. 1060 subtomogram volumes of MT singlet (2 × binned, 2.84 Å/pixel) were cropped from 7 tomograms in WARP[74]. Helical symmetry was applied in subtomogram averaging to reduce the effect of missing wedges. The rise and twist were assumed to be 9.46 Å and 27.7° as described before[78,79]. The MT polarity was determined according to the previous protocol[78,79]. Central pair MT was considered as two independent MT singlets and subtomogram averaging was performed in the same way as MT singlet. Those averaged results were used to make segmentation. ChimeraX[80] was used to render the segmentation results and the supplementary videos.

Quantification and statistical analysis

Protein band intensity in immunoblot was quantified using Fiji software from three independent experiments. The signals of target proteins were normalized with that of control proteins. All statistical analysis was performed using GraphPad Prism 8.0. Raw values in the figures are shown as mean ± SD. Details of statistical methods are reported in the figure legends. Two-tailed *t*-test or two-sided Mann–Whitney *U* test were used to compare differences between experiment groups. The number of samples, experiment replication information, and statistical significance values are shown in the figures.

Reporting summary

Further information on research design is available in the Nature Portfolio Reporting Summary linked to this article.

Data availability

The tomograms obtained in this study have been deposited at the Electron Microscopy Data Bank (EMDB) with accession numbers: EMD-64509, EMD-64510, and EMD-64508. All relevant data in this study are submitted as supplementary source files. Source data are provided with this paper.

References

1. World Health Organization. *World Malaria Report 2024* (WHO 2024).
2. Billker, O. et al. Calcium and a calcium-dependent protein kinase regulate gamete formation and mosquito transmission in a malaria parasite. *Cell* **117**, 503–514 (2004).
3. Sinden, R. E., Canning, E. U. & Spain, B. Gametogenesis and fertilization in Plasmodium yoelii nigeriensis: a transmission electron microscope study. *Proc. R. Soc. Lond. B Biol. Sci.* **193**, 55–76 (1976).
4. Bennink, S., Kiesow, M. J. & Pradel, G. The development of malaria parasites in the mosquito midgut. *Cell Microbiol.* **18**, 905–918 (2016).
5. Guttery, D. S., Roques, M., Holder, A. A. & Tewari, R. Commit and transmit: molecular players in Plasmodium sexual development and zygote differentiation. *Trends Parasitol.* **31**, 676–685 (2015).
6. Sinden, R. E., Talman, A., Marques, S. R., Wass, M. N. & Sternberg, M. J. The flagellum in malarial parasites. *Curr. Opin. Microbiol.* **13**, 491–500 (2010).
7. Sinden, R. E. Sexual development of malarial parasites. *Adv. Parasitol.* **22**, 153–216 (1983).
8. Sinden, R. E. Mitosis and meiosis in malarial parasites. *Acta Leiden.* **60**, 19–27 (1991).
9. Janse, C. J., Van der Klooster, P. F., Van der Kaay, H. J., Van der Ploeg, M. & Overdulve, J. P. Rapid repeated DNA replication during microgametogenesis and DNA synthesis in young zygotes of *Plasmodium berghei*. *Trans. R. Soc. Trop. Med. Hyg.* **80**, 154–157 (1986).
10. Rashpa, R. & Brochet, M. Expansion microscopy of Plasmodium gametocytes reveals the molecular architecture of a bipartite microtubule organisation centre coordinating mitosis with axoneme assembly. *PLoS Pathog.* **18**, e1010223 (2022).
11. Sinden, R. E., Canning, E. U., Bray, R. S. & Smalley, M. E. Gametocyte and gamete development in *Plasmodium falciparum*. *Proc. R. Soc. Lond. B Biol. Sci.* **201**, 375–399 (1978).
12. Klena, N. & Pigino, G. Structural biology of cilia and intraflagellar transport. *Annu. Rev. Cell Dev. Biol.* **38**, 103–123 (2022).
13. Satir, P. & Christensen, S. T. Overview of structure and function of mammalian cilia. *Annu. Rev. Physiol.* **69**, 377–400 (2007).
14. Carvalho-Santos, Z., Azimzadeh, J., Pereira-Leal, J. B. & Bettencourt-Dias, M. Evolution: tracing the origins of centrioles, cilia, and flagella. *J. Cell Biol.* **194**, 165–175 (2011).
15. Marshall, W. F. Basal bodies platforms for building cilia. *Curr. Top. Dev. Biol.* **85**, 1–22 (2008).
16. LeGuennec, M., Klena, N., Aeschlimann, G., Hamel, V. & Guichard, P. Overview of the centriole architecture. *Curr. Opin. Struct. Biol.* **66**, 58–65 (2021).
17. Greenan, G. A., Vale, R. D. & Agard, D. A. Electron cryotomography of intact motile cilia defines the basal body to axoneme transition. *J. Cell Biol.* **219**, e201907060 (2020).
18. Ostrowski, L. E., Dutcher, S. K. & Lo, C. W. Cilia and models for studying structure and function. *Proc. Am. Thorac. Soc.* **8**, 423–429 (2011).
19. Blanco-Ameijeiras, J., Lozano-Fernandez, P. & Marti, E. Centrosome maturation - in tune with the cell cycle. *J. Cell Sci.* **135**, jcs259395 (2022).
20. Sinden, R. E. The cell biology of malaria infection of mosquito: advances and opportunities. *Cell Microbiol.* **17**, 451–466 (2015).
21. Zeeshan, M. et al. Plasmodium SAS4: basal body component of male cell which is dispensable for parasite transmission. *Life Sci. Alliance* **5**, e202101329 (2022).
22. Stathatos, G. G., Dunleavy, J. E. M., Zenker, J. & O'Bryan, M. K. Delta and epsilon tubulin in mammalian development. *Trends Cell Biol.* **31**, 774–787 (2021).
23. Dutcher, S. K. Motile organelles: the importance of specific tubulin isoforms. *Curr. Biol.* **11**, R419–R422 (2001).
24. Dutcher, S. K. & Trabuco, E. C. The UNI3 gene is required for assembly of basal bodies of Chlamydomonas and encodes delta-tubulin, a new member of the tubulin superfamily. *Mol. Biol. Cell* **9**, 1293–1308 (1998).
25. Garreau de Loubresse, N., Ruiz, F., Beisson, J. & Klotz, C. Role of delta-tubulin and the C-tubule in assembly of Paramecium basal bodies. *BMC Cell Biol.* **2**, 4 (2001).
26. Dutcher, S. K., Morrissette, N. S., Preble, A. M., Rackley, C. & Stanga, J. Epsilon-tubulin is an essential component of the centriole. *Mol. Biol. Cell* **13**, 3859–3869 (2002).

27. Dupuis-Williams, P. et al. Functional role of epsilon-tubulin in the assembly of the centriolar microtubule scaffold. *J. Cell Biol.* **158**, 1183–1193 (2002).
28. Chang, P., Giddings, T. H. Jr, Winey, M. & Stearns, T. Epsilon-tubulin is required for centriole duplication and microtubule organization. *Nat. Cell Biol.* **5**, 71–76 (2003).
29. Ross, I., Clarissa, C., Giddings, T. H. Jr & Winey, M. epsilon-tubulin is essential in Tetrahymena thermophila for the assembly and stability of basal bodies. *J. Cell Sci.* **126**, 3441–3451 (2013).
30. Morrissette, N., Abbaali, I., Ramakrishnan, C. & Hehl, A. B. The tubulin superfamily in apicomplexan parasites. *Microorganisms* **11**, 706 (2023).
31. Lasonder, E. et al. Integrated transcriptomic and proteomic analyses of P. falciparum gametocytes: molecular insight into sex-specific processes and translational repression. *Nucleic Acids Res.* **44**, 6087–6101 (2016).
32. Yeoh, L. M., Goodman, C. D., Mollard, V., McFadden, G. I. & Ralph, S. A. Comparative transcriptomics of female and male gametocytes in *Plasmodium berghei* and the evolution of sex in alveolates. *BMC Genomics* **18**, 734 (2017).
33. Guan, J. et al. An axonemal intron splicing program sustains Plasmodium male development. *Nat. Commun.* **15**, 4697 (2024).
34. Sayers, C. et al. Systematic screens for fertility genes essential for malaria parasite transmission reveal conserved aspects of sex in a divergent eukaryote. *Cell Syst.* **15**, 1075–1091.e1076 (2024).
35. Louvel, V. et al. iU-ExM: nanoscopy of organelles and tissues with iterative ultrastructure expansion microscopy. *Nat. Commun.* **14**, 7893 (2023).
36. Wingfield, J. L. & Lechtreck, K. F. Chlamydomonas basal bodies as flagella organizing centers. *Cells* **7**, 79 (2018).
37. Dutcher, S. K. Elucidation of basal body and centriole functions in Chlamydomonas reinhardtii. *Traffic* **4**, 443–451 (2003).
38. Yang, S. et al. EB1 decoration of microtubule lattice facilitates spindle-kinetochore lateral attachment in Plasmodium male gametogenesis. *Nat. Commun.* **14**, 2864 (2023).
39. Alvarez Viar, G. et al. Protofilament-specific nanopatterns of tubulin post-translational modifications regulate the mechanics of ciliary beating. *Curr. Biol.* **34**, 4464–4475.e4469 (2024).
40. Job, D., Valiron, O. & Oakley, B. Microtubule nucleation. *Curr. Opin. Cell Biol.* **15**, 111–117 (2003).
41. Guichard, P., Chretien, D., Marco, S. & Tassin, A. M. Procentriole assembly revealed by cryo-electron tomography. *EMBO J.* **29**, 1565–1572 (2010).
42. Zhang, C. et al. Efficient editing of malaria parasite genome using the CRISPR/Cas9 system. *mBio* **5**, e01414 (2014).
43. Rawlings, D. J. et al. Alpha-tubulin II is a male-specific protein in *Plasmodium falciparum*. *Mol. Biochem. Parasitol.* **56**, 239–250 (1992).
44. Loreng, T. D. & Smith, E. F. The central apparatus of cilia and eukaryotic flagella. *Cold Spring Harb. Perspect. Biol.* **9**, a028118 (2017).
45. Straschil, U. et al. The Armadillo repeat protein PF16 is essential for flagellar structure and function in Plasmodium male gametes. *PLoS ONE* **5**, e12901 (2010).
46. Hirono, M. Cartwheel assembly. *Philos. Trans. R Soc. Lond. B Biol. Sci.* **369**, 20130458 (2014).
47. Kitagawa, D. et al. Structural basis of the 9-fold symmetry of centrioles. *Cell* **144**, 364–375 (2011).
48. Gopalakrishnan, J. et al. Sas-4 provides a scaffold for cytoplasmic complexes and tethers them in a centrosome. *Nat. Commun.* **2**, 359 (2011).
49. Marques, S. R. et al. An essential role of the basal body protein SAS-6 in Plasmodium male gamete development and malaria transmission. *Cell Microbiol.* **17**, 191–206 (2015).
50. Hatzopoulos, G. N. et al. Structural analysis of the G-box domain of the microcephaly protein CPAP suggests a role in centriole architecture. *Structure* **21**, 2069–2077 (2013).
51. Carvalho-Santos, Z. et al. Stepwise evolution of the centriole-assembly pathway. *J. Cell Sci.* **123**, 1414–1426 (2010).
52. Bettencourt-Dias, M. & Glover, D. M. Centrosome biogenesis and function: centrosomics brings new understanding. *Nat. Rev. Mol. Cell Biol.* **8**, 451–463 (2007).
53. Vasquez-Limeta, A. & Loncarek, J. Human centrosome organization and function in interphase and mitosis. *Semin. Cell Dev. Biol.* **117**, 30–41 (2021).
54. Turk, M. & Baumeister, W. The promise and the challenges of cryo-electron tomography. *FEBS Lett.* **594**, 3243–3261 (2020).
55. Sun, S. Y. et al. Cryogenic electron tomography reveals novel structures in the apical complex of *Plasmodium falciparum*. *mBio* **15**, e0286423 (2024).
56. Martinez, M. et al. Rhoptry secretion system structure and priming in *Plasmodium falciparum* revealed using in situ cryo-electron tomography. *Nat. Microbiol.* **7**, 1230–1238 (2022).
57. Ferreira, J. L. et al. Variable microtubule architecture in the malaria parasite. *Nat. Commun.* **14**, 1216 (2023).
58. Guichard, P. et al. Cartwheel architecture of Trichonympha basal body. *Science* **337**, 553 (2012).
59. Klena, N. et al. Architecture of the centriole cartwheel-containing region revealed by cryo-electron tomography. *EMBO J.* **39**, e106246 (2020).
60. Azimzadeh, J. & Bornens, M. Structure and duplication of the centrosome. *J. Cell Sci.* **120**, 2139–2142 (2007).
61. Hodges, M. E., Scheumann, N., Wickstead, B., Langdale, J. A. & Gull, K. Reconstructing the evolutionary history of the centriole from protein components. *J. Cell Sci.* **123**, 1407–1413 (2010).
62. Ikegami, K. & Setou, M. Unique post-translational modifications in specialized microtubule architecture. *Cell Struct. Funct.* **35**, 15–22 (2010).
63. Brito, C., Serna, M., Guerra, P., Llorca, O. & Surrey, T. Transition of human gamma-tubulin ring complex into a closed conformation during microtubule nucleation. *Science* **383**, 870–876 (2024).
64. Schmidt-Cernohorska, M. et al. Flagellar microtubule doublet assembly in vitro reveals a regulatory role of tubulin C-terminal tails. *Science* **363**, 285–288 (2019).
65. Takeda, Y. et al. Molecular basis promoting centriole triplet microtubule assembly. *Nat. Commun.* **15**, 2216 (2024).
66. Raabe, A. C., Wengelnik, K., Billker, O. & Vial, H. J. Multiple roles for *Plasmodium berghei* phosphoinositide-specific phospholipase C in regulating gametocyte activation and differentiation. *Cell Microbiol.* **13**, 955–966 (2011).
67. Talman, A. M. et al. Proteomic analysis of the Plasmodium male gamete reveals the key role for glycolysis in flagellar motility. *Malar. J.* **13**, 315 (2014).
68. Gao, H. et al. ISP1-anchored polarization of GCbeta/CDC50A complex initiates malaria ookinete gliding motility. *Curr. Biol.* **28**, 2763–2776.e2766 (2018).
69. Mastronarde, D. N. Automated electron microscope tomography using robust prediction of specimen movements. *J. Struct. Biol.* **152**, 36–51 (2005).
70. Eisenstein, F. et al. Parallel cryo electron tomography on in situ lamellae. *Nat. Methods* **20**, 131–138 (2023).
71. Hagen, W. J. H., Wan, W. & Briggs, J. A. G. Implementation of a cryo-electron tomography tilt-scheme optimized for high resolution subtomogram averaging. *J. Struct. Biol.* **197**, 191–198 (2017).
72. Zheng, S. Q. et al. MotionCor2: anisotropic correction of beam-induced motion for improved cryo-electron microscopy. *Nat. Methods* **14**, 331–332 (2017).

73. Kremer, J. R., Mastronarde, D. N. & McIntosh, J. R. Computer visualization of three-dimensional image data using IMOD. *J. Struct. Biol.* **116**, 71–76 (1996).
74. Tegunov, D. & Cramer, P. Real-time cryo-electron microscopy data preprocessing with Warp. *Nat. Methods* **16**, 1146–1152 (2019).
75. Liu, Y.-T. et al. Isotropic reconstruction for electron tomography with deep learning. *Nat. Commun.* **13**, 6482 (2022).
76. Scheres, S. H. RELION: implementation of a Bayesian approach to cryo-EM structure determination. *J. Struct. Biol.* **180**, 519–530 (2012).
77. Ermel, U. H., Arghittu, S. M. & Frangakis, A. S. ArtiaX: an electron tomography toolbox for the interactive handling of sub-tomograms in UCSF ChimeraX. *Protein Sci.* **31**, e4472 (2022).
78. Li, Z. et al. Cryo-electron tomography of Toxoplasma gondii indicates that the conoid fiber may be derived from microtubules. *Adv. Sci.* **n/a**, 2206595 (2023).
79. Li, W. et al. Integrated multimodality microscope for accurate and efficient target-guided cryo-lamellae preparation. *Nat. Methods* **20**, 268–275 (2023).
80. Pettersen, E. F. et al. UCSF ChimeraX: structure visualization for researchers, educators, and developers. *Protein Sci.***30**, 70–82 (2021).

Acknowledgements

We thank Prof. Friedrich Frischknecht (Heidelberg University), Prof. Kai Jiang (Wuhan University), Prof. Jingyan Fu (China Agricultural University), and Prof. Xin Liang (Tsinghua University) for the comments on this manuscript. We thank Dr. Qingfeng Liu (Xiamen University) for the help in the fluorescence imaging. We are grateful to the Cryo-EM Platform of Peking University, the National Centre for Protein Sciences at Peking University for technical assistance. This work was supported by the National Key Research and Development Program of China (2024YFC2309700), the National Natural Science Foundation of China (323B2020 by S.Y., 32170427 by J.Y. and 32270503 by H.C.), the 111 Project sponsored by the State Bureau of Foreign Experts and Ministry of Education of China (BP0618017 by J.Y.), the Xiamen University Double First Class Construction Project (Biology, DFC2024001 by J.Y.), and the Beijing Natural Science Foundation (JQ24031 by Q.G.). Q.G. is also supported by Changping Laboratory and the SLS-Qidong Innovation Fund.

Author contributions

S.Y., C.Y., and F.J. generated the modified parasites. S.Y. and C.Y. conducted the parasite phenotype analysis, IFA assay, image analysis, and mosquito experiments. S.M. and Z.L. performed the data collection of cryo-ET and image processing. S.Y. and L.Y. conducted the TEM experiments. H.C., Q.G., and J.Y. supervised the work. S.Y. and Y.J. wrote the manuscript.

Competing interests

The authors declare no competing interests.

Additional information

Supplementary information The online version contains supplementary material available at https://doi.org/10.1038/s41467-025-64158-8.

Correspondence and requests for materials should be addressed to Huiting Cui, Qiang Guo or Jing Yuan.

Peer review information *Nature Communications* thanks Linda Kohl, and the other, anonymous, reviewer(s) for their contribution to the peer review of this work. A peer review file is available.